CO 2 flow during orogenic gravitational collapse: Syntectonic decarbonation and fluid mixing at the ductile-brittle transition (Lavrion, Greece)

Christophe Scheffer, Alexandre Tarantola, Olivier Vanderhaeghe, Thomas Rigaudier, Adonis Photiades

To cite this version:

Christophe Scheffer, Alexandre Tarantola, Olivier Vanderhaeghe, Thomas Rigaudier, Adonis Photiades. CO 2 flow during orogenic gravitational collapse: Syntectonic decarbonation and fluid mixing at the ductile-brittle transition (Lavrion, Greece). Chemical Geology, 2017, 450, pp.248-263. ⟨10.1016/j.chemgeo.2016.12.005⟩. ⟨hal-02932271⟩

HAL Id: hal-02932271
https://hal.science/hal-02932271v1

Submitted on 6 Mar 2025

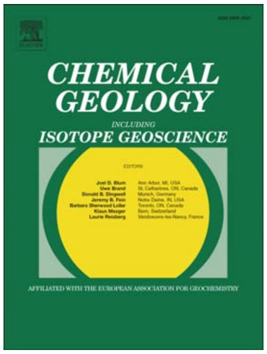

CO_2 flow during orogenic gravitational collapse: Syntectonic decarbonation and fluid mixing at the ductile-brittle transition (Lavrion, Greece)

Christophe Scheffer, Alexandre Tarantola, Olivier Vanderhaeghe, Thomas Rigaudier, Adonis Photiades

PII: S0009-2541(16)30654-4
DOI: doi:10.1016/j.chemgeo.2016.12.005
Reference: CHEMGE 18175

To appear in: *Chemical Geology*

Received date: 6 June 2016
Revised date: 21 November 2016
Accepted date: 3 December 2016

Please cite this article as: Scheffer, Christophe, Tarantola, Alexandre, Vanderhaeghe, Olivier, Rigaudier, Thomas, Photiades, Adonis, CO_2 flow during orogenic gravitational collapse: Syntectonic decarbonation and fluid mixing at the ductile-brittle transition (Lavrion, Greece), *Chemical Geology* (2016), doi:10.1016/j.chemgeo.2016.12.005

CO_2 flow during orogenic gravitational collapse: Syntectonic decarbonation and fluid mixing at the ductile-brittle transition (Lavrion, Greece)

Christophe Scheffer[1], Alexandre Tarantola[1], Olivier Vanderhaeghe[1-2], Thomas Rigaudier[3] and Adonis Photiades[4]

[1] *Université de Lorraine, CNRS, CREGU, GeoRessources UMR 7359, Faculté des Sciences et Technologies Boulevard Aiguillettes, Vandoeuvre-lès-Nancy, F-54506, France*

[2] *Université de Toulouse, Géosciences Environnement Toulouse (GET), UMR 5563 CNRS, 14 avenue Edouard Belin, Toulouse, F-31400, France.*

[3] *CRPG-CNRS, Université de Lorraine, UMR 7358, 15 rue Notre-Dame des Pauvres, BP 20, 54501 Vandoeuvre-lès-Nancy Cedex, France.*

[4] *Institute of Geology and Mineral Exploration (I.G.M.E.), 1st Spirou Louis St., Olympic Village, Acharnae 13677, Greece*

Keywords: CO_2, Decarbonation, Stable isotopes, Metamorphic Core Complex, Ductile-brittle transition, Cyclades.

ABSTRACT

The knowledge of CO_2 transfer between carbonate reservoirs is a key issue to understanding climate evolution through geologic times. Convergent plate boundaries represent major zones for carbon recycling via burial of carbonates. In this paper, we document syntectonic decarbonation of marble at the ductile-brittle transition during the emplacement of the low-angle mylonitic to cataclastic detachment exposed in the Lavrion peninsula along the western border of the Attico-Cycladic Metamorphic Complex. This process is evidenced by the presence, in a quartz vein boudinaged and transposed in the mylonitic marble, of CO_2-rich fluid inclusions (i) dismembered and deformed along quartz subgrain boundaries, (ii) within deformation lamellae and (iii) in planes crosscutting subgrains. Microstructural analysis, stable isotope equilibrium and *VX* properties show that CO_2 results from syntectonic decarbonation under a 70 to 115 °C.km^{-1} thermal gradient during exhumation accommodated by regional NNE-SSW extension. We propose that decarbonation and CO_2 release under HT/LP conditions were triggered by the increase in temperature caused by thermal relaxation of the thickened crust further enhanced by the intrusion of a granodiorite pluton during Miocene gravitational collapse of the Hellenic orogenic belt. Subsequent circulation of surface-derived fluid equilibrated with carbonaceous material of organic origin above the ductile-brittle transition led to precipitation of low ^{13}C carbonates. This study points that the production of CO_2 by syntectonic decarbonation of marble layers, representing tectonically accreted carbonates along convergent plate boundaries, should be considered in the carbon cycle and might thus impact the climate.

1. Introduction

Fluid production and flow in the Earth's crust can be reconstructed through careful microstructural and geochemical investigations of veins and fluid inclusions (e.g Küster and Stöckhert, 1997; Vapnik and Avigad, 2004; Eglinger et al., 2014; Diamond and Tarantola, 2015). Besides H_2O, CO_2 is a dominant volatile phase commonly observed in metamorphic fluids (Roedder, 1984; Crawford and Hollister, 1986; Diamond, 2001; Kerrick and Connolly, 2001; Yardley and Bodnar, 2014). The knowledge of carbon cycle is of primary importance in climate studies but also in reconstructing geological processes in various environments (Selverstone and Gutzler, 1993; Galvez et al., 2013; Ague and Nicolescu, 2014). The production of CO_2-rich fluids has been proposed to result from (i) redox reactions or interaction of fluids with carbonaceous material (e.g. French, 1966; Eugster and Skippen, 1967; Crawford and Hollister, 1986; Mullis, 1987; Touret, 2001; Tarantola et al., 2007, 2009), (ii) exsolution from mantle-derived magmas (e.g. Touret, 1971,1992; Schuiling and Kreulen, 1979) or (iii) decarbonation in calc-silicate rocks and carbonates associated with an increase of temperature (e.g. Valley, 1986; Baker et al., 1989; Boulvais et al., 1998; Bowman, 1998).

Convergent plate boundaries play a major role in the geochemical cycle of carbon through release of CO_2 at the Earth scale by metamorphic devolatilization (Barnes et al., 1978; Selverstone and Gutzler, 1993; Ague and Nicolescu, 2014) or by contamination of arc magmas by platform carbonates in the overlying crust and increased decarbonation efficiency (Johnston et al., 2011). Tectonically accreted carbonates in orogenic belts might also contribute to this cycle as they are subject to an increase in temperature owing to (i) an amplified contribution of radiogenic decay (England and Thompson, 1984; Vanderhaeghe et al., 2003), (ii) an augmented mantle heat flux caused by mantle delamination (Houseman et al., 1981) and/or (iii) magmatic underplating (Bergantz, 1989; Petford and Gallagher, 2001; Annen and Sparks, 2002; Fjeldskaar et al., 2003). These processes are not mutually exclusive and might act in concert for example in the case of slab retreat coeval with tectonic accretion of crustal units decoupled from a downgoing slab (Vanderhaeghe and Duchêne, 2010). The Hellenides-Aegean belt represents an emblematic example of construction and collapse of an orogenic belt along the Africa-Eurasia converging plate boundary marked by slab retreat (Jolivet et al., 1994; Gautier et al., 1999; Ring et al., 2010; Vanderhaeghe, 2012; Jolivet et al., 2013; Faccenna et al., 2014). In this context, increase in temperature leads to partial melting of the orogenic root as attested by numerous Miocene plutons (Keay et al., 2001; Iglseder et al., 2009; Liati et al., 2009; Bolhar et al., 2010) and by the Naxos and Paros migmatite domes exhumed in the central part of the Attico-Cycladic Metamorphic Complex, ACMC in a context of gravitational collapse (Fig.1a) (Vanderhaeghe and Teyssier, 2001; Vanderhaeghe, 2004; Duchêne et al., 2006; Kruckenberg et al., 2011). CO_2-rich fluid inclusions in quartz segregations and pegmatites in Naxos Island testify for large fluid production during high grade conditions (Rye et al., 1976; Schuiling and Kreulen, 1979; Kreulen, 1980, 1988; Baker et al., 1989; Buick and Holland, 1991; Siebenaller et al., 2013).

During the development of a Metamorphic Core Complex, the rocks are progressively cooled owing to exhumation marking the ductile-brittle transition (DBT). The fluid record of an exhumed metamorphic rock shows first trapping of metamorphic and/or magmatic fluids associated with ductile deformation and then entrapment of surface-derived fluids along fractures illustrating the transition from the deep ductile reservoir to the upper crustal brittle reservoir (Siebenaller et al., 2013; Dyja et al., 2016). Isotopic evidences suggest that superficial fluids can penetrate the crust down to the ductile crust along low-angle or high angle faults that are rooted into low-angle normal faults (e.g. Kerrich et al., 1984; Wickham et al., 1993; Morrison, 1994; Upton et al., 1995; Ingebritsen and Manning, 1999; Famin et al., 2004; Famin et al., 2005; Siebenaller et al., 2013; Menzies et al., 2014; Dyja et al., 2016). Below the DBT, fluids of the deep crust reservoir are confined under lithostatic conditions and their redistribution is intimately linked to intracrystalline deformation (Siebenaller et al., 2016) whereas, above the DBT, fluids of the upper crust reservoir are submitted to alternating lithostatic and hydrostatic conditions (Morrison and Anderson, 1998; Famin et al., 2005; Siebenaller et al., 2013; Dyja et al. 2016). As such, because the DBT zone is a place of change in the pressure regime and of fluid mixing, it appears as a strategic target to decipher fluid-rock interactions and exchanges between fluids reservoirs.

Our study contributes to this debate by depicting the fluid record of metamorphic rocks during deformation within a deformed quartz vein situated in the low-angle detachment exposed in the Lavrion peninsula (western boundary of the ACMC, Fig.1a). Marbles and metapelites exposed in the Lavrion area represent a former carbonate platform involved in the Hellenides orogenic belt at the boundary between the Africa and Eurasia converging plates (Dewey et al., 1973; Jolivet and Brun, 2010). This sedimentary sequence has been successively (i) dragged with the downgoing slab, (ii) tectonically accreted after decoupling from the slab, and (iii) tectonically exhumed to the surface by the emplacement of low-angle detachment which accommodates gravitational collapse (Scheffer et al., 2016). This last exhumation event is accommodated by the development of a mylonitic to cataclastic low-angle detachment mainly localized in marble layers (Scheffer et al., 2016). Major ore deposits took place in this particular context, with the development of a porphyry system associated to the emplacement of the Plaka granodiorite (Voudouris et al., 2008a,b; Bonsall et al., 2011). As such the Lavrion area represents a perfect target to study the syntectonic production/trapping of CO_2 during the different phases of orogenic evolution and the coeval input of magmatic and superficial fluids during exhumation through the DBT zone. CO_2 production by syntectonic decarbonation and fluid-rock interaction processes occurring at the DBT during exhumation are characterized by a combination of structural and microstructural observations, *VX* properties of fluid inclusions and stable isotope analyses.

2. Geological setting

2.1 Structure and petrology of lithotectonic units

The ACMC consists mainly of the Cycladic Blueschists that are partially or totally retrogressed into greenschist to amphibolite facies. These metamorphic rocks are overlain by the Pelagonian Unit delineated by a non-metamorphic ophiolitic mélange associated with Cretaceous limestones and have been exhumed along low-angle detachments during Miocene extension of the Aegean domain (Jolivet et al., 2010; Ring et al., 2010; Grasemann et al., 2012). The Lavrion peninsula is located about 40 km to the South East of Athens along the western boundary of the ACMC (Fig.1). The Lavrion peninsula exposes a stack of polyphased metamorphic nappes composed of, from top to bottom, (i) an upper unit dominated by the Lavrion schists, and (ii) a lower unit dominated by marbles alternating with the Kamariza schists (Fig.1b) (Photiades and Carras, 2001). The metamorphic rocks are locally unconformably overlain by non-metamorphosed lacustrian Miocene deposits.

The upper unit, also known as the phyllite nappe or the Lavrion Blueschists tectonic unit, is composed of a 100 to 250 m thick alternation of the Lavrion schists, including boudins of metavolcanites, and marbles. The Lavrion schists are rich in muscovite, quartz, albite, chlorite, glaucophane and epidote indicating greenschist to blueschist facies metamorphism (Baziotis et al., 2009). Two successive deformation-metamorphism phases at blueschist facies conditions have been distinguished by two chlorite-phengite assemblages using X-ray mapping on the Lavrion schists (Scheffer et al., 2016). D_1M_1 is characterized by a steep-dipping S_1 schistosity underlined by a first chlorite-phengite assemblage indicating 0.9-1.3 GPa and 315 +/- 30 °C, interpreted to record burial of a metasedimentary sequence dragged with a subducting slab. D_2M_2 is characterized by a steep-dipping S_2 schistosity marked by an E-W stretching lineation (Fig.1b) and a second chlorite-phengite assemblage showing an almost isothermal decompression (0.6-0.9 GPa, 300 +/- 30 °C) interpreted to record syn-orogenic exhumation. At the scale of the Cyclades, the H*P*/L*T* metamorphism occurred during Eocene (50-30 Ma) within the Cycladic Blueschists and reached conditions of 1.2 to 2.2 GPa and 450 to 550 °C (e.g. Altherr et al., 1982; Buick and Holland, 1989; Bröcker et al., 1993; Avigad, 1998; Trotet el al., 2001; Parra et al., 2002; Bröcker and Franz, 2005; Duchêne et al., 2006; Ring et al., 2007, 2011; Groppo et al., 2009).

The lower unit is composed of an at least 200 m thick alternation of folded marbles and the Kamariza schists. The Kamariza schists are rich in muscovite, quartz, albite and chlorite with granoblastic to lepidoblastic texture (Photiades and Carras, 2001). The lower unit is characterized by pervasive retrogression of the blueschist facies paragenesis into greenschist facies evidenced by two distinct chlorite-phengite assemblages of the Kamariza schists (Scheffer et al., 2016). Relics of early steep-dipping schistosity (S_{1-2}) reflecting a $D_{1-2}M_{1-2}$ event are locally preserved and show *P-T* conditions in blueschist facies (0.8-1.1 GPa, 280-320 °C) almost similar to the ones of the Lavrion schists. A last D_3M_3 event characterized by lower pressure conditions (0.50-0.85 GPa) associated with a slightly but significant higher temperature (350 +/- 30 °C) is responsible for the transposition of the previous S_{1-2} steep-dipping schistosity into a shallow-dipping S_3 schistosity bearing a NNE-SSW stretching lineation (Fig.1b). The D_3M_3 phase is interpreted to record post-orogenic exhumation of the thermally relaxed orogenic root (Scheffer et al., 2016). At the scale of the Cyclades, retrogression of blueschist facies into greenschist to amphibolite facies occurred between 25 and 15 Ma (Andriessen et al., 1979; Altherr et al., 1982; Ring et al., 2001; Ring and Reischmann, 2002; Duchêne et al., 2006; Seward et al., 2009).

The contact between the upper and lower units has been described as a low-angle detachment fault (Ring et al., 2007; Skarpelis et al., 2007; Liati et al., 2009; Lekkas et al., 2011; Berger et al., 2013; Scheffer et al., 2016). This low-angle detachment, which lies within the metamorphic nappe stack corresponds to the localization of the D_3 deformation underlined by a shallow-dipping mylonitic to cataclastic fabric marking the DBT during post-orogenic exhumation (Scheffer et al., 2016).

2.2 Plaka granodiorite intrusion and ore deposition

Intrusion of the Plaka granodiorite took place in this extensional context accommodated by the low-angle detachment (Pe-Piper and Piper, 2002). The crystallization of the granodiorite is dated at 8.34 +/- 0.2 Ma (1σ) by U-Pb on zircon (Liati et al., 2009). Relative rapid cooling of the pluton is constrained by K-Ar ages at 8.27 +/- 0.11 Ma on biotite and at 7.3 Ma by apatite fission track (Altherr et al., 1982). Aeromagnetic data suggest that the Plaka pluton represents the exposed part of a larger batholith present at a depth of 600 to 700 m below the surface of the Lavrion peninsula (Marinos and Makris, 1975; Tsokas et al., 1998). The emplacement of this large batholith is potentially responsible for the genesis and circulation of metal-rich fluids leading to major ore deposition (Skarpelis, 2002; Voudouris et al., 2008a, b; Bonsall et al., 2011).

2.3 Fluid inclusion investigations

Fluid inclusion investigations have been motivated in the Lavrion for the understanding of ore deposits and were performed within quartz, calcite, and fluorite gangue minerals (Mitsaki, 1972; Kalogeropoulos and Mitropoulos, 1983; Knoll, 1988; Skarpelis et al., 2007; Voudouris et al., 2008a, b; Bonsall et al., 2011). These authors suggested that a hot salt-rich fluid exsolved from the Plaka granodiorite, unmixed on cooling at 270-360 °C into a salt richer (>35 mass% $NaCl_{eq.}$) and a salt poorer (<25 mass% $NaCl_{eq.}$) end-member. On the basis of fluid inclusion data and isotopic signatures ($\delta^{13}C$, $\delta^{18}O$ and $\delta^{34}S$) of gangue minerals, this fluid was shown to be subsequently diluted by meteoric or marine water (Tombros et al. 2010), the resulting fluid having an average salinity of 14-18 mass% $NaCl_{eq}$. No traces of volatile components were identified within these fluids. Mixing between the different fluids contributed to successive deposits starting with porphyry-style deposits followed by carbonate replacement (Voudouris et al., 2008a, b; Bonsall et al., 2011). These studies suggest that boiling took place around 28 MPa, i.e. corresponding to a depth of 1.2 km (assuming lithostatic conditions), whereas carbonate replacement occurred at a minimal pressure of 3.5 MPa, (330 to 360 m depth), considering hydrostatic conditions (Voudouris et al., 2008a; Bonsall et al., 2011).

3. Methodology

3.1 Field strategy and sampling

Samples were systematically oriented on the field, in order to correlate quartz microstructure and fluid inclusion planes observed in thin and thick sections with the structural context. This study is based on a selected boudinaged quartz vein, representative of the numerous veins observed in the area, sampled at the intersection between marbles and schists alternations, a few meters below the low-angle detachment and in the vicinity of the Agios Konstantinos mine (sample CS02-006B, Fig.1b; N37°43'17.42" E24°0'43.18").

Thin and thick sections are oriented N005/70, so as to present a parallel section to the NNE-SSW stretching lineation that developed during post-orogenic exhumation (Scheffer et al., 2016).

3.2 Fluid inclusion analyses

Fluid inclusions were studied on double polished 200 µm-thick sections from the CS02-006B quartz vein. Because of the small size of the inclusions, the use of a spindle stage to measure the volume fraction of the non-aqueous phase was not possible (Bakker and Diamond, 2006). The area fraction a_{vap} (type IIb) and a_{car} (type I and IIa) of the non-aqueous phase was obtained on two-dimensional sections by area measurement using ImageJ (freeware obtainable at http://rsb.info.nih.gov). The orientation of fluid inclusion planes was performed on thick section using the Anima program (Lespinasse et al., 2005).

3.2.1 Microthermometry

Microthermometry measurements were performed at GeoRessources Laboratory (Université de Lorraine, Vandoeuvre-lès-Nancy, France) on a Linkam THMS600 heating-cooling stage. Natural water-rich CO_2 fluid inclusions hosted in Kyanite (Zambia) (H_2O-CO_2-NaCl, with T_m(car) = –56.6 °C) (Caumon et al., 2015), H_2O-NaCl and H_2O-NaOH synthetic fluid inclusions, with respectively T_e = –21.2 ° and T_m(ice) = –0.4 °C were used to calibrate the analytical device. The following phase transitions were measured when it was possible: T_m(car), final melting temperature of the carbonic phase, T_e, eutectic temperature which corresponds to the appearance of the first liquid from ice melting, T_m(ice), final melting temperature of ice, T_m(cla), dissociation temperature of clathrate at Q_2 conditions (Cla + L_{aq} + L_{car} + V_{car}), T_h(car), homogenization temperature of the carbonic phase (L_{car} + V_{car} = L_{car} or L_{car} + V_{car} = V_{car}), T_m(H) final melting of halite, and T_h, the bulk homogenization temperature (L_{aq} + L_{car} = L_{car} or L_{aq} + V_{aq} = L_{aq}).

Molar volume, salinity and composition of CO_2-rich fluid inclusions (types Ia and Ib) and aqueous fluid inclusions (type IIb) were calculated with the equations of state of Duan et al. (1992a,b) and Zhang and Frantz (1987) using Q2 and Bulk programs (Bakker 1997, 2003), respectively. These values were used to calculate the *P-T* isochoric curves with the equations of state of Anderko and Pitzer (1993a,b) and Duan et al. (1995) for type I and Knight and Bodnar (1989) and Bodnar and Vityk (1994) for type IIb using ISOC program (Bakker, 2003). Isochores of type IIa fluid inclusions are estimated assuming a H_2O-NaCl system using the equation from Bodnar and Vityk (1994).

3.2.2 Raman spectroscopy

Raman spectroscopy analyses were performed at GeoRessources Laboratory (Université de Lorraine, Vandoeuvre-lès-Nancy, France) on a Horiba Jobin-Yvon LabRAM HR laser-Raman spectrometer (exciting radiation at 514.532 nm; focal length 800 mm; 1 grating with 1,800 grooves per mm; 100 µm slit width; spectral resolution of 1.5 cm^{-1}; liquid N_2 cooled CCD) coupled with a Linkam THMS600 heating-cooling stage. The measurements were made just above the critical point of pure CO_2 (31.1 °C) to avoid any fractionation of the volatile components between the liquid and vapor phases.

3.3 Stable isotope measurements of calcite, quartz and CO_2

All isotopic measurements were performed at CRPG laboratory (Vandoeuvre-lès-Nancy, France). Isotopic measurements were systematically doubled in order to check homogeneity of analyses. Isotopic compositions are quoted in the standard delta notation in ‰ relative to V-PDB for carbon and converted to V-SMOW for oxygen.

3.3.1 Stable isotope measurements of calcite

Carbon and oxygen isotopic compositions of calcite were determined by using an auto sampler Gasbench coupled to a Thermo Scientific MAT253 isotope ratio mass spectrometer (IRMS). 250 to 300 µg of each carbonate sample was collected using a Dremel tool (1 mm diameter sampling hole). The obtained powder was then reacted with 2 mL of supersaturated orthophosphoric acid at 70 °C for at least 5 h in a He atmosphere. 10 measurement cycles of the produced CO_2 isotopic composition were performed with a Thermo Scientific MAT 253 continuous flow isotope ratio mass spectrometer. All sample measurements were adjusted to the internal reference calibrated on the international standards IAEA CO-1, IAEA CO-8 and NBS 19.

3.3.2 Oxygen isotope measurements of quartz

Oxygen isotope analyses were carried out using the conventional technique of Clayton and Mayeda (1963). Quartz vein was mechanically reduced to a grain size of 1-5 mm. Five milligrams of quartz grains were dried at 110 °C for 3 h, then loaded into a nickel reaction vessel, out-gassed under vacuum at room temperature for 2 h prior to reaction with BrF_5 at 600 °C for 10 h. The liberated O_2 was passed over a hot graphite rod to be converted into CO_2 for mass spectrometric measurement. Isotopic measurements were conducted on a Thermo-Fisher MAT253 Mass Spectrometer.

3.3.3 Stable isotope measurements of CO_2 from fluid inclusions

Quartz vein was reduced to a grain size of 5-10 mm. For each sample, 1-5 g of quartz grains were loaded into a stainless steel tube and out-gassed overnight under vacuum at 120 °C. Quartz grains were then crushed and the liberated H_2O and CO_2 were collected in a liquid nitrogen cold trap at –170 °C. Non-condensable volatiles (e.g. H_2, O_2, CH_4 and N_2) were evacuated. In order to separate CO_2 from H_2O, the liquid nitrogen trap was warmed up to –80 °C. The liberated CO_2 was collected for mass spectrometric measurement. Isotopic measurements were conducted on a Thermo-Fisher MAT253 Mass Spectrometer.

3.3.4 Isotopic fractionation

In order to discuss equilibrium between calcite and CO_2 from fluid inclusions, the fractionation equations from Ohmoto and Rye (1979) and Zheng (1999) were applied to carbon and oxygen isotopic values at specific temperatures. Calcite-graphite fractionation equation from Bottinga (1969) was used at specific temperatures to discuss the origin of low $\delta^{13}C$ isotopic signatures.

4. Results

4.1 Structural position of quartz and calcite veins

Brown-orange carbonate veins rich in iron oxides are systematically observed within and up to a few meters below the detachment fault in the vicinity of the mineralized area (Agios Konstantinos, Thorikos, Megala Pefka) within the mylonitic marble of the lower unit. They are observed both crosscutting and concordant to the S_3 mylonitic fabric of the marble (Fig.2a). Pole projection orientations of the veins crosscutting S_3 indicate a system of conjugate normal faults consistent with a NNE-SSW direction of extension (Fig.2b).

The boudinaged quartz vein was sampled within the Kamariza schists of the lower unit (Fig.2c). The vein, found some sixty meters away from the main entrance of the Agios Konstantinos mining gallery in a level showing alternations (S_0) of schists and mylonitic marbles, is transposed into the shallow-dipping S_3.

4.2 Petrography and microstructures

The sampled quartz vein is concordant to the foliation of the schists and marbles host rock and is pinched and swelled indicating that it has been transposed into the shallow-dipping S_3 mylonitic fabric. Quartz microstructure is characterized by undulatory extinction, subgrain boundary, bulging (BLG), subgrain rotation recrystallization (SGR) and lamellar deformation (Fig.3a-e). Kinematic criteria such as lamellar bands decorated with fluid inclusions (Fig.3d) testify a top-to-the-SSW sense of shear.

Calcite crystals forming the marble layer have a homogeneous size (250 µm on average) with 120° triple junctions typical of a mosaic equilibrium texture acquired during dynamic recrystallization (Urai et al., 1986). They display a shape preferred orientation filling the neck in between quartz pinched layers (Fig.3a-b).

Brown-orange calcite crystallized in microcracks rooted at the tip of the marble layer that has filled the gap in the boudin's neck (Fig.3a-b) and in fractures crosscutting the quartz vein and the marble. The 200 µm to 1 mm crystals are heterogeneous and show subhedral shapes. The brown-orange color is probably due to the presence of numerous Fe, Zn and Mn oxides, often associated with phyllosilicates. The brown-orange calcite and calcite from marble are characterized by type I to II twins (Ferrill et al., 2004).

4.3 Fluid inclusion petrography

Two types, containing each 2 sub-types, of fluid inclusions are distinguished within the quartz vein.

Types Ia and Ib are three-phase CO_2-rich characterized by aqueous liquid (L_{aq}), carbonic liquid (L_{car}) and vapor (V_{car}) at room temperature. Type Ia inclusions (Fig.4a) are the most abundant. These 5 to 30 µm inclusions can have deformed or rounded to crystal negative shape. At room temperature, the carbonic phase (a_{car}) is around 80 vol.% and dominated by carbonic liquid. Type Ia are (i) dismembered (Fig.3c; Diamond et al., 2010; Tarantola et al., 2010, 2012; Diamond and Tarantola, 2015), (ii) accumulated along quartz subgrain boundaries (Fig.3c; Kerrich, 1976; Wilkins and Barkas, 1978), (iii) distributed as ‘en-echelon’ short trails along deformation lamellae (Fig.3d; Böhm, 1883; Vernooij and Langenhorst, 2005), or (iv) in planes crosscutting quartz subgrains (Fig.3e).

Type Ib inclusions (Fig.4b) are rare (only five planes identified in the thick section) and are systematically trapped along transgranular secondary planes crosscutting quartz subgrains and grains. They show rounded to crystal negative shape, with a mean size around 10 µm. Type Ib is also characterized by three-phase CO_2-rich fluid inclusions at room temperature but their a_{car} is higher than 90 vol.% and dominated by carbonic vapor.

The orientation of types Ia and Ib fluid inclusion planes (respectively 86 and 5 measurements) reveals two poles (Fig.4e) at N291/51 and N114/75. The bisector angle of 53° suggests that these planes are conjugate faults indicating micro-cracking according to a NNE-SSW direction of extension.

Type IIa inclusions are rare, small (between 3 and 12 µm), with rounded to crystal negative shapes (Fig.4c). Only ten inclusions were found, always within type IIb fluid inclusion planes. They are aqueous dominated $L_{aq}L_{car}V_{car}$ fluid inclusions with a_{car} ~20 vol.%, and contain halite (Hal) and one or two daughter solids (S_1, S_2) that are too small to be identified by Raman spectroscopy.

Type IIb are two-phase $L_{aq}V_{car}$ aqueous fluid inclusions with a_{car} around 15 vol.% (Fig.4d). They display a variety of shapes from rounded to elongated parallel to the fluid inclusion plane and some are decrepitated. Their size range from a few µm up to more than 50 µm.

Type II fluid inclusions are systematically distributed along transgranular planes, without any preferred orientation, crosscutting the quartz vein and the marble (Fig.3f), subgrains and planes filled by type I fluid inclusions. Type II fluid inclusion planes (94 measurements) show heterogeneous distribution (Fig.4f) without any specific organization.

4.4 Fluid inclusion geochemistry

4.4.1 Microthermometry

Microthermometry data are reported in Table 1. Type Ia and type Ib carbonic fluid inclusions show the same T_m(car) from –57.8 to –56.5 °C (presence of three phases V_{car}, L_{car}, L_{aq}). Moreover, T_m(cla) are roughly similar for both types of inclusions, with temperatures respectively between 7.0 and 9.7 °C and 9.1 and 10.3 °C via a quadruple (Q_2) point (presence of four phases V_{car}, L_{car}, L_{aq} and clathrate).

Beside these similarities type Ia and type Ib carbonic fluid inclusions are distinguished by their T_h(car) and T_h. Type Ia are characterized by a T_h(car) ranging between 29.1 and 30.4 °C always by disappearance of the carbonic vapor phase and a T_h occurring around 340 °C ($L_{aq} + L_{car} = L_{car}$). Type Ib are characterized by a T_h(car) between 21.0 and 29.2 °C, always by disappearance of the aqueous liquid phase and T_h occurred between 295 and 300 °C ($L_{aq} + L_{car} = L_{car}$).

Type IIa aqueous carbonic fluid inclusions are characterized by the following phase transitions. T_e of the aqueous part was measured between –56.9 to –52.9 °C suggesting the presence of $CaCl_2$ and NaCl in the aqueous solution. T_m(car) occurred at –56.7 °C (presence of three phases V_{car}, L_{car}, L_{aq}). T_h(car) was measured between 28.6 and 29.6 °C always by disappearance of the carbonic vapor phase. T_m(H) occurred between 140 and 160 °C. T_h occurred at temperatures above 350 °C.

Type IIb aqueous inclusions are observed at a T_e between –33.5 and –21.2 °C, suggesting a solution mainly dominated by NaCl. T_m(ice) was measured between –12.0 and –1.3 °C. Finally T_h occurred between 156 and 298 °C ($L_{aq} + V_{aq} = L_{aq}$).

4.4.2 Raman spectroscopy

Raman spectroscopy data are reported in Table 2. The vapor phase of all types of fluid inclusions are dominated by CO_2 with various amounts of CH_4, N_2, H_2 and H_2S.

The gas phase of type Ia and type Ib is dominated by CO_2 (respectively 98.8 to 99.5 mol% and 98.1 to 99.4 mol%), with minor amount of CH_4 (0.3 to 0.8 mol% and 0.3 to 1.2 mol%) and N_2 (0.0 to 0.6 mol% and 0.1 to 1.0 mol%) with always the presence of H_2S up to 0.1 mol% (the band at 2611 cm^{-1} is very weak but always visible) and possible traces of H_2.

The gas phase of type IIa aqueous-carbonic fluid inclusions is dominated by CO_2 (97.7 to 99.8 mol%) with minor amount of CH_4 (0.1 to 2.0 mol%) and N_2 (0.0 to 0.2 mol%) and traces of H_2. Daughter minerals entrapped within type I fluid inclusions are too small to be accurately identified by Raman spectroscopy (≤ 1 µm).

The gas phase of type IIb aqueous fluid inclusions also shows the predominance of CO_2 (96.4 to 99.5 mol%), with minor N_2 (0.1 to 3.0 mol%), CH_4 (0.1 to 1.1 mol%), H_2 (0.0 to 0.5 mol%) and rare traces of H_2S.

4.4.3 Fluid inclusion VX properties

The gas phase is largely dominated by CO_2 as suggested T_m(car) and T_m(cla) data and Raman spectroscopy (always higher than 98.0 mol% for type I and 96.0 mol.% for type II). In order to work with more robust equations of state, fluid inclusion *VX* properties were calculated assuming pure CO_2 in the carbonic phase and NaCl as the only salt species (salinity given as $NaCl_{eq.}$).

According to clathrate dissociation temperatures and CO_2 density, the salinity is in the range 3.2-8.0 mass% $NaCl_{eq.}$ for type Ia and 2.4-4.3 mass% $NaCl_{eq.}$ for type Ib. Bulk molar volume is in the range 45.3-47.4 $cm^3.mol^{-1}$ for type Ia and 105.0-142.0 $cm^3.mol^{-1}$ for type Ib.

For type IIa, halite melting temperatures indicate a salinity ranging between 29.5 and 30.3 mass% $NaCl_{eq.}$ (Sterner et al., 1988). For type IIb, the salinity given by ice melting is in the range 2.2 to 16.0 mass% $NaCl_{eq.}$ (Bodnar, 1993) and bulk molar volume is in the range 19.8-25.0 $cm^3.mol^{-1}$.

4.5 Stable isotopes

$\delta^{13}C$ and/or $\delta^{18}O$ stable isotopes were analyzed on quartz, the different generations of calcite, and fluid inclusions (Fig.5; Table 3).

The $\delta^{18}O$ signature of the surrounding quartz vein is comprised between 24.2 and 24.5 ‰ $_{V\text{-}SMOW}$.

Calcite, which composes the folded marble layer at the base of the thin section (Fig.3a), shows $\delta^{13}C$ comprised between –0.2 and 1.7 ‰ $_{V\text{-}PDB}$, and a $\delta^{18}O$ between 19.2 and 21.4 ‰ $_{V\text{-}SMOW}$. This range is relatively close to the one of marine limestone defined by Bowman (1998). The brown-orange calcite observed at the thin section scale shows a high depletion in ^{13}C (–4.2 ‰ $_{V\text{-}PDB}$) and a weak enrichment in ^{18}O (24.6 to 25.0 ‰ $_{V\text{-}SMOW}$). Additional brown-orange calcite veins sampled at the Lavrion scale, trapped during ductile to brittle deformation within and below the detachment fault (e.g Fig.2a), show $\delta^{13}C$ between –4.6 and –10.0 ‰ $_{V\text{-}PDB}$ and $\delta^{18}O$ between 23.1 and 25.5 ‰ $_{V\text{-}SMOW}$.

As it was not possible to separate mechanically the different types of fluid inclusions, the isotopic signature of CO_2 ($\delta^{13}C$ from 2.6 to 2.7 ‰ $_{V\text{-}PDB}$ and $\delta^{18}O$ from 31.9 to 33.8 ‰ $_{V\text{-}SMOW}$) corresponds to the bulk fluid from the vein. However, because type I inclusions have the higher CO_2 density and are the most abundant in the quartz vein, we assume that at least 98 % of the measured bulk CO_2 can be attributed to this specific population.

5. Discussion

In this discussion, the veins and their fluid inclusions are replaced in the structural context at the scale of the Lavrion area. The source of the CO_2 and of the brown-orange calcite is discussed on the basis of isotopic equilibrium. The *VX* properties of the fluid permit understanding fluid flow and entrapment conditions. Overall, circulation of CO_2-rich fluids is compared with other case studies at the Attico-Cycladic scale, and allows generalizing syntectonic decarbonation during gravitational collapse. Finally, the process and the possible heat sources are discussed.

5.1 Structural to microstructural recording

The structure and metamorphic assemblage of the marbles and schists alternations exposed in the Lavrion peninsula record the successive stages of the tectonic evolution of the ACMC, namely (i) burial during subduction, (ii) syn-orogenic exhumation associated with tectonic construction of the orogenic belt, and (iii) post-orogenic exhumation during orogenic gravitational collapse accommodated by a shallow-dipping detachment interpreted to represent localized deformation at the DBT (Scheffer et al., 2016). Below and within this detachment, marbles and schists are partially or totally transposed within the S_3 shallow-dipping schistosity developed during NNE-SSW extension. This story has been partially recorded in the boudinaged quartz vein presented in this paper. Indeed, the vein is totally transposed within S_3 at the transition between marble and schists sampled a few meters below the low angle detachment fault indicating an emplacement before the development of S_3 (Fig.6a). Intracrystalline deformation of quartz (undulose extinction, presence of subgrains and lamellae) and recrystallization by bulging and subgrain rotation are consistent with a ductile deformation at a temperature between 280 and 450 °C (Hirth and Tullis, 1992; Stöckhert et al., 1999; Stipp et al., 2002a,b; Passchier and Trouw, 2006), in agreement with temperature recorded by schists during the development of S_3 (Scheffer et al., 2016). The deformation evolves from ductile to brittle conditions as suggested by (i) the dynamic recrystallization of the quartz vein and the calcite from the marble, (ii) the mylonitic deformation recorded by the marble, (iii) the boudinaged shape of the quartz vein, (iv) the ductile creep of the marble between quartz pinched layers and (v) the brittle cracks crosscutting the marble and the quartz vein filled by the brown-orange calcite. This structural-microstructural evolution is attributed to decreasing *P*-*T* conditions owing to exhumation of metamorphic rocks beneath the shallow-dipping detachment.

The asynchronous ductile-brittle behavior during deformation of the marble and the quartz vein reflects the contrast of competence between calcite and quartz (Ramsey, 1983). This is consistent with experimental deformation indicating that at temperature above 350 °C, calcite and quartz are both ductile, and that the temperature corresponding to the ductile-brittle transition is lower for quartz than calcite (Urai et al., 1986; Cartner and Tsenn, 1987; Hirth and Tullis, 1992; 1994; Kohlstedt et al., 1995).

The microstructural position of Type I fluid inclusions within the quartz vein is evidence of continuous entrapment during exhumation across the DBT in a general context of NNE-SSW extension (Fig.6b-e). Type II fluid inclusions, trapped only within crosscutting trails, postdate type I fluid inclusions and record the transition to brittle deformation (Fig.6e-f). Their heterogeneous orientation suggests that they are the result of hydraulic fracturing.

5.2 Origin of CO_2-rich fluid and aqueous dominated fluids

The $\delta^{13}C$ values (2.7 ± 0.1 ‰ $_{V\text{-}PDB}$) of the CO_2 from the fluid inclusions trapped in quartz correspond to the signature of the fluid at the time of trapping. Indeed, unlike oxygen of CO_2, which is likely modified by partial equilibration with entrapped water and the host quartz, there cannot be interaction and fractionation between carbon and quartz. $\delta^{13}C$ values of CO_2 are neither consistent with an organic carbonaceous material (< –20 ‰ $_{V\text{-}PDB}$, eg. Kreulen, 1988) nor a mantle source (–1.6 to –10.8 ‰ $_{V\text{-}PDB}$, eg. Trull et al., 1993). Because the isotopic values of CO_2 are higher than the carbonate host-rock, a magmatic contribution is also not likely (Fig.5). Accordingly the mylonitic marble is the most probable source for CO_2. The isotopic signature of calcite from the mylonitic marble is marked by a significant fractionation compared to the marine limestone signature and shows a trend with a strong depletion in ^{13}C and a weak depletion in ^{18}O. In comparison, CO_2 is weakly enriched in ^{13}C and strongly enriched in ^{18}O (Fig.5). These features are pointing to a production of carbon dioxide by decarbonation of marble (Valley, 1986; Boulvais et al., 1998; Bowman, 1998). The equilibrium temperature indicated by the ^{13}C fractionation ranges between 256 and 454 °C (Ohmoto and Rye, 1979). The temperatures of the decarbonation process are thus consistent with the conditions admitted to the ductile to brittle deformation of quartz. Type IIa fluid inclusions show striking similarities with magmatic fluid inclusions found in pyrite-molybdenite quartz veins from porphyry-style mineralization in Plaka (Voudouris et al., 2008a; Bonsall et al., 2011). The only significant difference is the presence of CO_2 that could be explained either by interactions with the carbonate host-rock or mixing with type I CO_2-rich fluid inclusions. Type IIb fluid inclusions have been reported in quartz, calcite and fluorite of the Kamariza area (Voudouris et al., 2008b; Bonsall et al., 2011) and are interpreted as late meteoric and/or marine fluids that dilute magmatic fluids issued from the crystallization of the Plaka granodiorite.

5.3 Origin of low ^{13}C brown-orange calcite

The ^{13}C depleted values (down to –10‰ $_{\text{V-PDB}}$) measured in brown-orange calcite from the outcrop to the thin section scale (Fig.5) are clearly out of equilibrium with the marbles of the Lavrion nappes and suggest inflow of an external fluid. As almost all carbonate rocks in the Lavrion area have a δ^{13}C and δ^{18}O isotopic signature ranging between the marine limestone box and the magmatic box (Bonsall et al., 2011; Berger et al., 2013), the occurrence of low ^{13}C calcite veins could not be realistically explained by decarbonation of depleted ^{13}C carbonates. CO_2 fluid inclusions from ultramafic xenolith were shown to have δ^{13}C signatures from –1.6 to –10.8 ‰ $_{\text{V-PDB}}$ (Trull et al., 1993). For our temperatures of interest, i.e. between 450 and 200 °C, calcite with a contribution from mantle-derived CO_2 should thus display a δ^{13}C between –1.2 to 10.6 ‰ $_{\text{V-PDB}}$ according to Ohmoto and Rye (1979). These δ^{13}C signatures thus preclude a mantellic contribution to the formation of brown-orange calcite

(Fig.5). Alternatively, these low ^{13}C values can point to an organic contribution as already suggested in Cycladic islands for similar brown-orange carbonate veins (Rye et al., 1976; Kreulen, 1980; Matthews and Schliestedt, 1984; Baker et al., 1989; Ganor et al., 1994). Carbonaceous material with δ^{13}C comprised between –27 to –9 ‰ $_{\text{V-PDB}}$ with a mode at –25 to –20 ‰ $_{\text{V-PDB}}$ has been described in Naxos Island (Kreulen, 1988, 1989), but was not highlighted in the Lavrion area. Oxidation of carbonaceous material by an oxidizing aqueous fluid, as suggested by Ganor et al. (1994), could explain the origin of ^{13}C depleted brown-orange calcite veins. Assuming a carbonaceous material with a δ^{13}C signature of –25 to –20 ‰ $_{\text{V-PDB}}$, the derived calcite would show a δ^{13}C between –17.0 to –5.8 ‰ $_{\text{V-PDB}}$ for temperatures between 450 and 200 °C according to Bottinga (1969). These values would thus be in agreement with the low ^{13}C signatures of brown-orange calcite. Another hypothesis is that low δ^{13}C calcite comes from the infiltration of meteoric fluid carrying soil CO_2 dissolved at low temperature (Hendy, 1971; Bar-Matthews et al., 1991; Ganor et al., 1994; Boulvais et al., 2007). In absence of evidence of carbonaceous material of organic origin in the Lavrion nappe pile, this proposition provides an alternative for the source of low δ^{13}C brown-orange calcite. This is consistent with the characteristics of this vein network indicating precipitation after exhumation of the host rocks across the DBT at the time of penetration of surficial fluids (Type IIb).

5.4 Fluid flow at the ductile to brittle transition

In order to simplify the system for *PVTX* calculations and to use better constrained equations of states, the carbonic phase for all fluid inclusions was considered as being made of pure CO_2 (in any case higher than 96 mol%, Table 2). Bulk molar volumes of type Ia inclusions are in the range 45.3-47.4 cm^3.mol^{-1} while type Ib are characterized by higher molar volumes (105.0-142.0 cm^3.mol^{-1}).

Because of their high CO_2 content, the isochores (Fig.7a) of Ia and Ib fluid inclusions have a weak $\Delta P/\Delta T$ evolution. Moreover, they appear parallel to geothermal gradients of 70 to 115 °C.km^{-1} considering lithostatic (type Ia) or hydrostatic pressure regime (type Ib).

This observation supports the fact that type I fluid inclusions were trapped continuously, along the same geothermal gradient, from high temperature during ductile deformation under lithostatic pressure (type Ia) to lower temperature during brittle deformation under a hydrostatic pressure (type Ib). The exact maximum temperature is not constrained and depends likely on the proximity to the heat source, namely the Plaka granodiorite intrusion. Nevertheless, CO_2-carbonate equilibrium indicates, for this specific vein, a temperature as high as 454 °C.

This change of pressure regime from lithostatic to hydrostatic is in agreement with petrographic position of Type Ia fluid inclusions trapped at the DBT, as shown by plastically deformed fluid inclusion planes, and type Ib trapped during brittle deformation. These isochores mark the progressive exhumation of rocks across the DBT during the emplacement of the low-angle detachment which accommodates orogenic gravitational collapse (Fig.7b). At the DBT, type Ia carbonic fluid inclusions were trapped at a mean pressure around 110 MPa corresponding to a depth around 4000 m under lithostatic pressure. Type Ib carbonic fluid inclusions were trapped at a mean pressure around 34 MPa corresponding to a depth around 3400 m considering hydrostatic pressure.

No valid equation of state exist in the literature to accurately calculate molar volume of type IIa fluid inclusions. As a guess, the isochores are drawn considering a H_2O-NaCl system using the equation of Bodnar and Vityk (1994) for halite saturated systems. The homogenization temperatures are at 350 to 400 °C by Voudouris et al. (2008a,b) and Bonsall et al. (2011) for similar fluid inclusions. Isochores of type IIa suggest high temperature fluid circulation without thermal equilibrium with the host-rocks (Fig.7a). Fluid exsolution from the granodiorite is the more likely source (Bonsall et al., 2011). The emplacement of the Plaka granodiorite was estimated at a depth of 1.2 km from fluid inclusions measured at 280 bars assuming a lithostatic pressure (Bonsall et al., 2011). Because these fluid inclusions are found within crosscutting trails, they would have been more likely trapped under a hydrostatic pressure regime. As such, the corresponding depth would be around 2800 m, more in agreement with our estimation.

Isochores of type IIb fluid inclusions are also plotted in Figure 7. Hot magmatic fluids (type IIa) were first trapped at temperatures higher than 350 °C and progressively diluted by the arrival of surficial fluids, which record the end of the exhumation history. Two extreme exhumation paths can then be proposed. The first one (path 3a) corresponds to isobaric cooling of the host rocks followed by slow exhumation along a mean geothermal gradient of 30 $°C.km^{-1}$ under hydrostatic pressure regime. The second one (path 3b) corresponds to exhumation to the surface following the same geothermal gradient (70 to 115 $°C.km^{-1}$). The actual path is likely localized between these two extreme solutions (Fig.7a).

5.5 Syntectonic decarbonation at the Attico-Cycladic scale?

CO_2 flow during retrograde path in the ACMC was also highlighted by fluid inclusions analysis in Naxos Island (Kreulen, 1980, 1988, 1989; Siebenaller et al., 2013), Tinos Island (Famin et al., 2004; 2005) or by Perplex modelling in Syros Island (Kleine et al., 2014). CO_2-rich fluid inclusions trapped within quartz veins within the lower greenschist unit in Tinos Island are characterized by similar chemical properties (T_h, T_m(cla), T_h(car)) than type I. Nevertheless, they show a lower a_{car} (between 0.4 and 0.6 vol.%), and are thus characterized by steeper isochores suggesting a lower geothermal gradient than those measured within our type I trapped in the Lavrion lower unit (Fig.8). Similarly, CO_2-rich fluid inclusions trapped between 280-320 °C and 40-120 MPa at lithostatic to hydrostatic pressure conditions at the DBT was mentioned in Naxos Island (Siebenaller et al., 2013). The range of $\delta^{13}C$ signature of CO_2-rich fluid inclusions trapped in Naxos Island is –16 to +5 ‰ $_{V\text{-}PDB}$ and is also interpreted as a proof of decarbonation of marble and interactions with carbonaceous material (Rye et al., 1976; Kreulen, 1980, 1988; Baker et al., 1989). The systematic observation of CO_2-rich fluid circulation at the ductile-brittle transition, during exhumation, supports large scale syntectonic decarbonation during orogenic gravitational collapse.

At the scale of the Cyclades, the increase in temperature recorded by the lowest structural level of the ACMC is potentially induced by the combined effects of (i) an increased radioactive heat production in the thickened crust, and (ii) an increased basal heat flux caused by asthenospheric upwelling in response to slab retreat, and (iii) heat advection induced by the emplacement of mantle-derived magmas (Vanderhaeghe et al., 2007). This increase in temperature reaches its climax in Naxos Island as suggested by the presence of migmatites (Duchêne et al., 2006; Martin et al., 2008; Kruckenberg et al., 2011). In the Lavrion area, the exposed structural level is probably not as deep as in the central part of the Cyclades (Scheffer et al., 2016) but contact metamorphism is detected around the Plaka granodiorite that might have induced dehydration and decarbonation and thus CO_2 volatilization. A fast frictional heating during shearing at the transition from ductile to brittle deformation could also be invoked. Such a model of fast seismic slip causing frictional heating (reaching 800 °C) within clays and carbonates leading H_2O and CO_2 production by dehydration and decarbonation reaction has been proposed for the Naukluft low-grade (< 200 °C) thrust fault (Namibia) (Rowe et al., 2012).

6. Conclusions

A combination of structural, microstructural, fluid inclusion and stable isotope analyses performed on a boudinaged quartz vein transposed within a low-angle detachment fault in the Lavrion area (Greece) allowed characterizing fluid genesis and fluid-rock interaction processes at the DBT induced by the post-orogenic exhumation of the ACMC. This study has shown that:

(i) CO_2-rich fluid entrapment and low $\delta^{13}C$ calcite crystallization are associated to NNE-SSW extension accommodating Miocene post-orogenic exhumation of the ACMC. These processes both occurred at the DBT at temperatures of 450 °C to 250 °C.

(ii) CO_2-rich fluid with positive $\delta^{13}C$ is generated by syntectonic decarbonation of tectonically accreted marble induced by the increase in temperature affecting marble in a ductile closed system. The transition from ductile to brittle deformation is marked by the end of the decarbonation and by the percolation of magmatic fluids exsolved from the granodioritic magma.

(iii) Finally, the exhumation of rocks across the DBT exposed them to the percolation of surface-derived fluid equilibrated in the upper crust with carbonaceous material leading to the precipitation of low $\delta^{13}C$ brown-orange calcite. The transition from the ductile closed system to a brittle open system took place at a depth of 3.4-4.0 km. This is associated with a change of the pressure regime (lithostatic to hydrostatic) for a geothermal gradient ranging from 70 to 115 °C.km^{-1}. The HT/LP conditions are consistent with fluid entrapment during gravitational collapse of a thermally relaxed orogenic crust including heat input from the Plaka granodiorite.

(iv) Similar CO_2-rich fluid inclusions and low ^{13}C brown-orange carbonate veins both trapped during the post-orogenic retrograde path in several Island from the ACMC probably attests to a large scale process.

(v) In the same way as carbonate subduction can release large amount of CO_2 during subduction (Ague and Nicolescu, 2014, Johnston et al., 2011), we propose that syntectonic decarbonation during post-orogenic collapse represents a complementary process to consider in the global carbon cycle (Kelemen and Manning, 2015) and thus should be considered as a potential agent of climate change.

Acknowledgments

Field trips in Lavrion were made possible by work permits delivered by IGME in Athens. The city of Lavrion is thanked for providing access to the Technological Park and its housing facilities. We thank Panagiotis Voudouris for his helpful and discussion on the field. We also thank Marie-Camille Caumon for their assistance with Raman spectroscopy.

This work has been financially supported by the CNRS-INSU CESSUR, OTELO and Labex Ressources21. We take this opportunity to thank Marie-Odile Campadieu and Nathalie Carol for smooth bookkeeping of financial credits, Alexandre Flammang for conscientious thin section elaboration. This work is part of the PhD thesis of Christophe Scheffer who acknowledges a fellowship from the French Ministry of Education and Research and is grateful for the warm welcome at the GeoRessources laboratory in Nancy. The authors are also grateful M. Galvez, U. Ring, and V. Famin for their helpful and pertinent comments and Michael E. Böttcher for efficient editorial handling.

Figure Captions

Figure 1. a. Structural map of the western part of the Attico-Cycladic Metamorphic Complex (ACMC) at the junction between the Hellenic belt and the Aegean domain showing the spatial distribution of the Cycladic Blueschists Unit. The North Cycladic Detachment System

(NCDS) and the West Cycladic Detachment System (WCDS) observed in Lavrion area (this study), accommodate post-orogenic exhumation of the Cycladic Blueschists Unit. Modified after Jacobshagen (1986); Grasemann et al. (2012); Berger et al. (2013) and Augier et al. (2015). **b.** Geological map of the Lavrion peninsula (modified after Photiades and Carras, 2001 and Scheffer et al., 2016). Equal angle Wulff net stereographic projection (lower hemisphere) of stretching lineation of the upper unit in blue, and of the lower unit in green. The number of measurements (n) is indicated.

Figure 2.a. Brown-orange calcite veins concordant to and cross-cutting the mylonitic marble suggesting a trapping during DBT (N 37°43'14.00"; E 24°1'58.97"). **b.** Equal angle Wulff net stereographic projection (lower hemisphere) of carbonate crosscutting veins, showing a setting up as tension gashes, perpendicular to the NNE-SSW stretching direction. **c.** The boudinaged quartz vein (CS02-006B) sampled at the Agios Konstantinos mining (N37°43'17.42"; E 24°0'43.18") at 4.5 km to the south of the Plaka granodiorite outcrop is transposed within the S_3 schistosity at the intersection between marble and schist alternations.

Figure 3.a. Thick section (N 37°43'17.42"; E 24° 0'43.18") parallel to the NNE-SSW stretching lineation showing ductile creep of marble into a neck into a boudinaged quartz vein. Brown-orange calcite fills microcracks rooted at the extremity of the marble layer. Blue squares and orange diamonds correspond respectively to the location of in-situ stable isotope analyses of marble and brown-orange calcite given in Fig.5 and Table 3. **b.** Detail of mylonitic calcite from the deformed marble layer under cross polarized light showing shape preferred orientation into the quartz boudin’s neck and the sharp transition with brown-orange calcite. **c.** Photograph under cross polarized light of type Ia CO_2-rich fluid inclusions partially deformed along quartz subgrain boundaries. Bulging (BLG) and subgrain rotation (SGR) of

quartz is indicated. **d.** Photograph under plane polarized light of type Ia CO_2-rich fluid inclusions emphasizing deformed sigmoidal quartz lamellae deformation indicating a top-to-the-SSW sense of shear. **e.** Photograph under cross polarized light of type Ia CO_2-rich fluid inclusions both crosscutting and partially deformed along quartz subgrain boundaries. **f.** Photograph under plane polarized light of type II aqueous fluid inclusions crosscutting quartz and calcite from the marble.

Figure 4.a. Three phase type Ia CO_2-rich fluid inclusion dominated by carbonic liquid. **b.** Three phase type Ib CO2-rich fluid inclusion dominated by carbonic vapor. **c.** Multiphase type IIa halite saturated aqueous-carbonic fluid inclusion **d.** Two phase type IIb aqueous fluid inclusion. **e.** Equal angle Wulff net stereographic projection (lower hemisphere) showing the orientation of type I CO_2-rich fluid inclusion planes Ia (black dots) and Ib (red dots), respectively 86 and 5 measurements. Two pole projections (green dots) at N291/51 and N114/75 correspond to the average orientation of the planes. The bisector angle of 53° suggests that these planes are conjugate faults consistent with a NNE-SSW extension direction. **f.** Equal angle Wulff net stereographic projection (lower hemisphere) of type II aqueous fluid inclusions suggest a trapping in a cataclastic domain. H.: halite, L_{aq}: aqueous liquid, L_{car}: carbonic liquid, V_{car}: carbonic vapor, S_1 and S_2: unidentified solids.

Figure 5. $\delta^{13}C$ vs. $\delta^{18}O$ composition of marble, brown-orange calcite, quartz and type I CO_2-rich fluid. Points 1 to 5 refer to the sample location given in Fig.3a. Blue squares are calcite from the mylonitic marble measured at the thin section scale. Red circle is ype I CO_2-rich fluid. Orange diamonds are brown-orange calcite measured at the thin section scale. Brown diamonds are those measured at the outcrop scale. The marine limestone and igneous boxes after Bowman (1998) are indicated. The mantle box is from Trull et al. (1993). All isotope

values are normalized to Vienna Pee Dee Belemnite (V-PDB) and Vienna Standard Mean Ocean Water (V-SMOW). See Table 3.

Figure 6. Synthetic reconstruction of fluid generation and successive trapping events within the quartz vein related to the rheological evolution during post-orogenic exhumation. **a.** Mylonitic ductile deformation accommodated by intracrystalline deformation responsible for the transposition of $S_{1/2}$ into a S_3 shallow-dipping schistosity. **b, c, d.** Lithostatic decarbonation of marble and type Ia (in red) trapping coeval with ductile to brittle deformation of quartz (affected by intracrystalline deformation and fractures) and ductile deformation of marble. **e.** Hydrostatic decarbonation and type Ib (in purple) trapping associated with brittle deformation of quartz and ductile to brittle deformation of marble. Precipitation of brown-orange calcite is induced by the progressive percolation of surface-derived fluid equilibrated with carbonaceous material. **f.** Circulation of magmatic and surface-derived fluids (Type II in black and blue respectively) during brittle deformation marked by the precipitation of brown-orange calcite.

Figure 7a. *P-T* trapping conditions of type I and II fluid inclusions calculated using ISOC program (Bakker, 2003). The DBT domain for quartz is represented by a light grey field. Type Ia fluid inclusions (red isochores) were trapped at lithostatic pressure in the ductile domain for a geothermal gradient range between 70 and 90 $°C.km^{-1}$ (step 1). The isochores are parallel to this geothermal gradient. Type Ib fluid inclusions (purple isochores) were trapped at hydrostatic pressure at the DBT for a geothermal gradient range between 70 and 115 $°C.km^{-1}$ (step 2). Type IIa fluid inclusions (dark grey isochores field) were trapped at high temperature in hydrostatic regime. Type IIb fluid inclusions (blue isochores) were trapped in hydrostatic regime and under two possible scenarios (i) a progressive isobaric decrease of temperature without exhumation (3a) or (ii) an exhumation path following a constant geothermal gradient (3b). **b.** Synthetic *P*-*T* paths recorded in the Lavrion area. D_1M_1, D_2M_2 and D_3M_3 are from Scheffer et al. (2016). The late D_3M_4 episode is marked by a local increase of temperature correlated to the vicinity of the Plaka granodiorite intrusion

Figure 8. Comparison between the *P*-*T* paths recorded in the Lavrion area (in black) and those proposed in Tinos (dark grey) and Naxos Island (light grey) are given by Parra et al. (2002) and Duchêne et al. (2006) respectively. Isochores of CO_2-rich fluid trapped during the retrograde path in Tinos and Naxos Island are given in dark grey from Famin et al. (2004) and light grey from Siebenaller et al. (2013) respectively. Isochores of CO_2-rich fluid inclusion (Type I) trapped in the Lavrion area are represented by the pink field.

Table Captions

Table 1. Microthermometric results of type I and II fluid inclusions. First line of each type gives the data range; the second line the average value, the number of analyses is given between brackets. n.c.: not calculated because no equation of state for this type of fluid inclusion is published in the literature (halite saturated CO_2-rich fluid inclusions). All data are given with a maximum error of +/- 0.1 °C.

Table 2. Gas proportion (mol%) of the non-aqueous phase of the different fluid inclusion types obtained by Raman spectroscopy. First line of each type gives the data range, the second line the average and the number of analyses is given between brackets. n.d.: not detected.

Table 3. Stable isotope composition ($\delta^{13}C$ and $\delta^{18}O$) of mylonitic marble, quartz vein, brown-orange calcite and CO_2 from fluid inclusions performed both on the thin section (Points 1 to 5, see Fig. 3a) and the outcrop scale. Isotopic measurements were systematically doubled in order to check homogeneity of measurements.

References

Altherr, R., Kreuzer, H., Wendt, I., Lenz, H., Wagner, G.A., Keller, J., Harre, W., Hohndorf, A., 1982. A late Oligocene/early Miocene high temperature belt in the Attic–Cycladic crystalline complex (SE Pelagonian, Greece). Geologisches Jahrbuch E23, 97–164.

Annen, C., Sparks, R.S.J., 2002. Effects of repetitive emplacement of basaltic intrusions on thermal evolution and melt generation in the crust. Earth and Planetary Science Letters 203, 937-955.

Ague, J.J., Nicolescu, S., 2014. Carbon dioxide released from subduction zones by fluid-mediated reactions. Nature Geoscience 7, 355–360.

Anderko, A., Pitzer, K.S., 1993a. Equation-of-state representation of phase equilibria and volumetric properties of the system NaCl-H_2O above 573 K. Geochimica et Cosmochimica Acta 57, 1657–1680.

Anderko, A., Pitzer, K.S., 1993b. Phase equilibria and volumetric properties of the system KCl-H_2O and NaCl-KCl-H_2O above 573 K. Geochimica et Cosmochimica Acta 57, 4885–4897.

Andriessen, P.A.M., Boelrijk, N.A.J.M., Hebeda, E.H., Priem, H.N.A., Verdurmen, E.A.T., Verschure, R.H., 1979. Dating the events of metamorphism and granitic magmatism in the Alpine Orogen of Naxos (Cyclades, Greece). Contributions to Mineralogy and Petrology 69, 215–225.

Avigad, D., 1998. High-pressure metamorphism and cooling on SE Naxos (Cyclades, Greece). European Journal of Mineralogy 10 (6), 1309–1319.

Augier, R., Jolivet, L., Gadenne, L., Lahfid, A., Driussi, O., 2015. Exhumation kinematics of the Cycladic Blueschists unit and back-arc extension, insight from the Southern Cyclades (Sikinos and Folegandros Islands, Greece). Tectonics 34, 152–185.

Baker, J., Bickle, M.J., Buick, I.S., Holland, T.J.B., Matthews, A., 1989. Isotopic and petrological evidence for the infiltration of water-rich fluids during the Miocene M2 metamorphism on Naxos, Greece. Geochimica et Cosmochimica Acta 53, 2037–2050.

Bakker, R.J., 1997. Clathrates: Computer programs to calculate fluid inclusion V-X properties using clathrate melting temperatures. Computers & Geosciences 23, 1–18.

Bakker, R.J., 2003. Package FLUIDS 1. Computer programs for analysis of fluid inclusion data and for modelling bulk fluid properties. Chemical Geology 194, 3–23.

Bakker, R.J., Diamond, L.W., 2006. Estimation of volume fractions of liquid and vapor phases in fluid inclusions, and definition of inclusion shapes. American Mineralogist 91, 635–657.

Bar-Matthews, M., Matthews, A., Ayalon, A., 1991. Environmental controls of speleothem mineralogy in a karstic dolomitic terrain (Soreq cave, Israel). The Journal of Geology 99, 189–207.

Barnes, I., Irwin, W.P., White, D.E., 1978. Global distribution of carbon dioxide discharges and major zones of seismicity. Water Resources Investigations report 78–39, 12 p.

Baziotis, I., Proyer, A., Mposkos, E., 2009. High-pressure/Low-temperature metamorphism of metabasites in Lavrion area (SE Attica Greece): implications for the preservation of peak metamorphic assemblages in blueschists and greenschists. European Journal of Mineralogy 21, 133–148.

Bergantz, G.W., 1989. Underplating and partial melting implications for melt generation and extraction, Science 254, 1039–1095.

Berger, A., Schneider, D.A., Grasemann, B., Stockli, D., 2013. Footwall mineralization during Late Miocene extension along the West Cycladic Detachment System, Lavrion, Greece. Terra Nova 25 (3), 181–191.

Bodnar, R.J., 1993. Revised Equation and Table for Determining the Freezing Point Depression of H2O-NaCl Solutions. Geochimica et Cosmochimica Acta 57, 683–684.

Bodnar, R.J., Vityk, M.O., 1994. Interpretation of microthermometric data for H_2O-NaCl fluid inclusions. In Inclusions in Minerals, Methods and Applications, B. De Vivo and M.L. Frezzotti, eds., pub. By Virginia Tech, Blacksburg, VA, 117–130.

Böhm, A., 1883. Ueber die Gesteine des Wechsels. Mineralogische und Petrographische Mitteilungen 4, 197–214.

Bolhar, R., Ring, U., Allen, C.M., 2010. An integrated zircon geochronological and geochemical investigation into the Miocene plutonic evolution of the Cyclades, Aegean Sea, Greece: Part 1: Geochronology. Contributions to mineralogy and petrology 160 (5), 719–742.

Bonsall, T.A., Spry, P.G., Voudouris, P.C., Tombros, S., Seymour, K.S., Melfos, V., 2011. The Geochemistry of Carbonate-Replacement Pb-Zn-Ag Mineralization in the Lavrion District, Attica, Greece: Fluid Inclusion, Stable Isotope, and Rare Earth Element Studies. Economic Geology 106, 619–651.

Bottinga, Y., 1969. Calculated fractionation factors for carbon and hydrogen isotope exchange in the system calcite-carbon dioxide-graphite-methane-hydrogen-water vapor. Geochimica et Cosmochimica Acta 33, 49–64.

Boulvais, P., Fourcade, S., Gruau, G., Moine, B., Cuney, M., 1998. Persistence of pre-metamorphic C and O isotopic signatures in marbles subject to Pan-African granulite-facies metamorphism and U–Th mineralization (Tranomaro, Southeast Madagascar). Chemical Geology 150, 247–262.

Boulvais, P., Brun, J.P., Sokoutis, D., 2007. Fluid circulation related to post-Messinian extension, Thassos Island, North Aegean. Geofluids 7, 159–170.

Bowman, J.R., 1998. Stable-isotope systematics of skarn. In: Lentz, D.R. (Ed.), Mineralized Intrusion-Related Skarn Systems. Mineralogical Association of Canada. Short Course 26, 99–145.

Bröcker, M., Franz, L., 2005. The base of the Cycladic blueschist unit on Tinos Island (Greece) re-visited: field relationships, phengite chemistry and Rb–Sr geochronology. Neues Jahrbuch für Mineralogie – Abhandlungen 181 (1), 81–93.

Bröcker, M., Kreuzer, H., Matthews, A., Okrusch, M., 1993. 40Ar/39Ar and oxygen isotope studies of polymetamorphism from Tinos Island, Cycladic blueschist belt, Greece. Journal of Metamorphic Geology 11, 223–240.

Buick, I.S., Holland, T.J.B., 1989. The P–T–t path associated with crustal extension,Naxos, Cyclades, Greece. Geological Society, London, Special Publications 43, 365–369.

Buick, I.S., Holland, T.J.B., 1991. The nature and distribution of fluids during amphibolite facies metamorphism, Naxos (Greece). Journal of Metamorphic Geology 9, 301–314.

Cartner, N.L., Tsenn, M.C., 1987. Flow properties of continental lithosphere. Tectonophysics 136, 27–63.

Clayton, R.N., Mayeda, T.K., 1963. The use of bromine pentafluoride in the extraction of oxygen from oxides and silicates for isotopic analysis. Geochemica and Cosmochimica Acta 27, 43–52.

Caumon, M.C., Tarantola, A., Mosser-Ruck, R., 2015. Raman spectra of water in fluid inclusions: I. Effect of host mineral birefringence on salinity measurement. Journal of Raman Spectroscopy 46(10), 969–976.

Crawford M. L., Hollister L. S., 1986. Metamorphic fluids: The evidence from fluid inclusions. In Fluid-Rock Interactions during Metamorphism (eds. J. V. Walther and B. J. Wood). Springer-Verlag, New York, pp. 1–35.

Dewey, J.F., Pitman, W.C., Ryan, W.B.F., Bonin, J., 1973. Plate tectonics and the evolution of the Alpine system. Geological Society of America Bulletin 84, 3137–3180.

Diamond, L., 2001. Review of the systematics of CO_2-H_2O fluid inclusions. Lithos 55, 69–99.

Diamond, L.W., Tarantola, A., Stunitz, H., 2010. Modification of fluid inclusions in quatz by deviatoric stress. II: experimentally induced changes in inclusion volume and composition. Contributions to mineralogy and petrology 160, 845–864.

Diamond L.W., Tarantola A., 2015. Interpretation of fluid inclusions in quartz deformed by weak ductile shearing: reconstruction of differential stress magnitudes and pre-deformation fluid properties. Earth and Planetary Science Letters 417, 107–119.

Duan, Z., Moller, N., Weare, J.H., 1992a. Prediction of methane solubilities in natural waters to high ionic strength from 0 to 250 C and from 0 to 1600 bar. Geochimica et Cosmochimica Acta 56, 1451–1460.

Duan, Z., Moller, N., Weare, J.H., 1992b. An equation of state for the CH_4–CO_2–H_2O system: I Pure systems for 0 to 1000 C and 0 to 8000 bar. Geochimica et Cosmochimica Acta 56, 2605–2617.

Duan, Z., Moller, N., Weare, J.H., 1995. Equation of state for the NaCl-H_2O-CO_2 system: prediction of phase equilibria and volumetric properties. Geochimica et Cosmochimica Acta 59, 2869–2882.

Duchêne, S., Aissa, R., Vanderhaeghe, O., 2006. Pressure-temperature-time evolution of metamorphic rocks from Naxos (Cyclades, Greece): constraints from thermobarometry and Rb/Sr dating. Geodinamica Acta 19, 301–321.

Dyja, V., Hibsch, C., Tarantola, A., Cathelineau, M., Boiron, M.C., Marignac, C., Bartier, D., Carrillo-Rosua, J., Morales, Ruano, S., Boulvais, P., 2016. From deep to shallow fluid reservoirs: Evolution of fluid sources during the exhumation of the Sierra Almagrera, Betic Cordillera, Spain. Geofluids 16, 103–128.

Eglinger, A., Ferraina, C., Tarantola, A., André-Mayer, A.S., Vanderhaeghe, O., Boiron, M.C., Dubessy, J., Richard, A., Brouand, M., 2014. Hypersaline fluids generated by high-grade metamorphism of evaporites: fluid inclusion study of uranium occurrences in the Western Zambian Copperbelt. Contributions to Mineralogy and Petrology 167 (2), 1–28.

England, P.C., Thompson, A.B., 1984. Pressure–temperature–time paths of regional metamorphism. I. Heat transfer during the evolution of regions of thickened continental crust. Journal of Petrology 25 (4), 894–928.

Eugster, H.P., Skippen, G.B., 1967. Igneous and metamorphic reactions involving gas equilibria, in Researches in Geochemistry, 2 , edited by L.S. Abelson, pp. 492–520. Wiley and Sons, New York.

Faccenna, C., Becker, T.W., Auer, L., Billi, A., Boschi, L., Brun, J.P., Capitanio, F.A., Funiciello, F., Horvàth, F., Jolivet, L., Piromallo, C., Royden, L., Rossetti, F., Serpelloni, E., 2014. Mantle dynamics in the Mediterranean. Reviews of Geophysics 52, 283–332.

Famin, V., Philippot, P., Jolivet, L., Agard, P., 2004. Evolution of hydrothermal regime along a crustal shear zone, Tinos Island, Greece. Tectonics 23, 1–23.

Famin, V., Hébert, R., Philippot, P., Jolivet, L., 2005. Ion probe and fluid inclusion evidence for co-seismic fluid infiltration in a crustal detachment. Contributions to Mineralogy and Petrology 150 (3), 354–367.

Ferrill, D.A., Morris, A.P., Evans, M.A., Burkhard, M., Groshong Jr, R.H., Onasch, C.M., 2004. Calcite twin morphology: a low-temperature deformation geothermometer. Journal of Structural Geology 26, 1521–1529.

Fjeldskaar, W., Johansen, H., Dodd, T.A., Thompson, M., 2003. Temperature and maturity effects of magmatic underplating in the Gjallar Ridge, Norwegian Sea, in S. Düppenbecker and R. Marzi, eds., Multidimensional basin modeling, AAPG/Datapages Discovery Series 7, 71–85.

French, B.M., 1966. Some geological implications of equilibrium between graphite and a C-H-O gas phases at high temperatures and pressures: Reviews of Geophysics 4, 223–253.

Galvez, M., Beyssac, O., Martinez, I., Benzerara, K., Chaduteau, C., Malvoisin, B., Malavieille, J., 2013. Graphite formation by carbonate reduction during subduction. Nature Geosciences 6, 473–477.

Ganor, J., Matthews, A., Schliestedt, M., 1994. Post metamorphic low δ13C calcite in the Cycladic Complex (Greece) and their implications for modeling fluid infiltration processes using carbon isotopic compositions. European Journal of Mineralogy 6, 365–379.

Gautier, P., Brun, J.P., Moriceau, R., Sokoutis, D., Martinod, J., Jolivet, L., 1999. Timing, kinematics and cause of Aegean extension: a scenario based on a comparison with simple analogue experiments. Tectonophysics 315, 31–72.

Grasemann, B., Schneider, D.A., Stockli, D.F., Iglseder, C., 2012. Miocene bivergent crustal extension in the Aegean: evidence from the western Cyclades (Greece). Lithosphere 4 (1), 23–39.

Groppo, C., Forster, M., Lister, G., Compagnoni, R., 2009. Glaucophane schists and associated rocks from Sifnos (Cyclades, Greece): New constraints on the P–T evolution from oxidized systems. Lithos, 109 (3), 254–273.

Hendy, C.H., 1971. The isotopic chemistry of speleothems. I. The calculation of the effects of different modes of formation on the isotopic composition of speleothems and their applicability as paleoclimatic indicators. Geochimica Cosmochimca Acta 35, 801–824.

Hirth, G., Tullis, J., 1992. Dislocation creep regimes in quartz aggregates. Journal of Structural Geology 18, 145–159.

Hirth, G., Tullis, J., 1994. The brittle-plastic transition in experimentally deformed quartz aggregates. Journal of geophysical research 99, 11731–11747.

Houseman, G.A., McKenzie, D.P., Molnar, P., 1981. Convective instability of a thickened boundary layer and its relevance for the thermal evolution of continental convergent belts. Journal of Geophysical Research B 86 (7), 6115–6132.

Iglseder, C., Grasemann, B., Schneider, D.A., Petrakakis, K., Miller, C., Klötzli, U.S., Thöni, M., Zámolyi, A., Rambousek, C., 2009. I and S-type plutonism on Serifos (W-Cyclades, Greece). Tectonophysics 473 (1–2), 69–83.

Ingebritsen, S.E., Manning, C.E., 1999. Geological implications of a permeability-depth curve for the continental crust. Geology 27 (12), 1107–1110.

Jacobshagen, V., 1986. Geologie von Griechenland. Borntraeger, Berlin-Stuttgart, pp. 363.

Johnston, F.K.B., Turchyn, A.V., Edmonds, M., 2011. Decarbonation efficiency in subduction zones: Implications for warm Cretaceous climates. Earth and Planetary Science Letters 303, 143–152.

Jolivet L., Brun J.P., Gautier P., Lallemant S., Patriat M., 1994. 3-D kinematics of extension in the Aegean from the Early Miocene to the Present, insight from the ductile crust, Bulletin de la Société géologique de France 165, 195–209.

Jolivet, L., Brun, J.P., 2010. Cenozoic geodynamic evolution of the Aegean. International Journal of Earth Sciences, Geologishe Rundschau 99, 109–138.

Jolivet, L., Lecomte, E., Huet, B., Denèle, Y., Lacombe, O., Labrousse, L., Le Pourhiet,L., Mehl, C., 2010. The north cycladic detachment system. Earth and Planetary Science Letters 289, 87–104.

Jolivet, L., Faccenna, C., Huet, B., Labrousse, L., Le Pourhiet, L., Lacombe, O., Lacomte,E., Burov, E., Denele, Y., Brun, J., Philippon, M., Paul, A., Salaun, B., Karabulut, H.,Piromallo, C., Monie, P., Gueydan, F., Okay, A., Oberhänsli, R., Pourteau, A.,Augier, R., Gadenne, L., Driussi, O., 2013. Aegean tectonics: strain localization slab tearing and trench retreat. Tectonophysics 597–598, 1–33.

Kalogeropoulos, S., Mitropoulos, P., 1983. Fluid inclusion characteristic of fluorite from Laurion (Greece). Annales Géologiques Des Pays Helleniques 31, 130–135.

Keay, S., Lister, G., Buick, I., 2001. The timing of partial melting, Barrovian metamorphism and granite intrusion in the Naxos metamorphic core complex, Cyclades, Aegean Sea, Greece. Tectonophysics 342 (3–4), 275–312.

Kelemen, P.B., Manning, C.E., 2015. Reevaluating carbon fluxes in subduction zones, what goes down, mostly comes up. Proceedings of the National Academy of Sciences 112, E3997-E4006.

Kerrich, R., 1976. Some effects of tectonic recrystallisation on fluid inclusions in vein quartz. Contributions to Mineralogy and Petrology 59, 195–202.

Kerrich, R., La Tour, T.E., Willmore, L., 1984. Fluid participation in deep fault zones: Evidence from geological, geochemical, and $^{18}O/^{16}O$ relations. Journal of Geophysical Research 89, 4331–4343.

Kerrick, D.M., Connolly, J.A.D., 2001. Metamorphic devolatilization of subducted marine sediments and the transports of volatiles into the Earth's mantle. Nature 411, 293–296.

Kleine, B., Skelton, A.D.L., Huet, B., Pitcairn, I.K., 2014. Preservation of Blueschist facies minerals along a shear zone by coupled metasomatism and fast-flowing CO_2-bearing fluids. Journal of Petrology 55 (10), 1905–1939.

Knight, C.L., Bodnar, R.J., 1989. Synthetic fluid inclusions. IX. Critical PVTX properties of NaCl-H_2O solutions. Geochimica and Cosmochimica Acta 53, 3–8.

Knoll, O., 1988. Ore mineralogy and fluid inclusion studies of Pb-Zn-ores from Lavrion-Greece. Thèse. University of Hambourg.

Kohlstedt, D.L., Evans, B., Mackwell, S.J., 1995. Strength of the lithosphere: Constraints imposed by laboratory experiments. Journal of Geophysical Research 100, 17587-17602.

Kreulen, R., 1980. CO2-rich fluids during regional metamorphism on Naxos (Greece): carbon isotopes and fluid inclusions. American Journal of Science 280, 745–771

Kreulen, R., 1988. High integrated fluid/rock ratios during metamorphism at Naxos; evidence from carbon isotopes of calcite in schists and fluid inclusions. Contributions to Mineralogy and Petrology 98, 28–32.

Kreulen, R., 1989. Fluid/rock ratios during metamorphism at Naxos: reply. Contributions to Mineralogy and Petrology 103, 127–129.

Kruckenberg, S.C., Vanderhaeghe, O., Ferré, E.C., Teyssier, C., Whitney, D.L., 2011. Flow of partially molten crust and the internal dynamics of a migmatite dome, Naxos, Greece. Tectonics 30, TC3001.

Küster, M., Stöckhert, B., 1997. Density changes of fluid inclusions in high-pressure low-temperature metamorphic rocks from Crete: A thermobarometric approach based on the creep strength of the host minerals. Lithos 41, 151–167.

Lekkas, S., Skourtsos, E., Soukis, K., Kranis, H., Lozios, S., Alexopoulos, A., Koutsovitis, P. 2011. Late Miocene detachment faulting and crustal extension in SE Attica (Greece). European Geosciences Union, General Assembly, 3-8 April 2011, Vienna, Austria.

Lespinasse, M., Désindes, L., Fratczak, P., Petrov, V., 2005. Microfissural mapping of natural cracks in rocks: Implications for fluid transfers quantification in the crust. Chemical Geology 223, 170–178.

Liati, A., Skarpelis, N., Pe-Piper, G., 2009. Late Miocene magmatic activity in the Attic-Cycladic belt of the Aegean (Lavrion, SE Attica, Greece): implications for the geodynamic evolution and timing of ore deposition. Geological Magazine 146, 732–742.

Marinos, G., Makris, J., 1975. Geological and geophysical considerations of new mining operations in Laurium, Greece. Annales Geologiques des Pays Helléniques 27, 1–10.

Martin, L., Duchêne, S., Deloule, E., Vanderhaeghe, O., 2008. Mobility of trace elements and oxygen in zircon during metamorphism: consequences for geochemical tracing. Earth and Planetary Science Letters 267 (1–2), 161–174.

Matthews, A., Schliestedt, M., 1984. Evolution of the blueschist and greenschist facies rocks of Sifnos, Cyclades, Greece. Contributions to Mineralogy and Petrology 88, 150–163.

Menzies, C.D., Teagle, D.A. H., Craw, D., Cox, S.C., Boyce, A.J., Barrie, C.D., Roberts, S., 2014. Incursion of meteoric waters into the ductile regime in an active orogen. Earth and Planetary Science Letters 399, 1–13.

Mitsaki, V., 1972. Geochemical investigation of hydrothermal-pneumatolitic fluorites from Greece. Unpublished Ph.D. thèse.

Morrison, J., 1994. Meteoric water-rock interaction in the lower plate of the Whipple Mountain metamorphic core complex, California. Journal of metamorphic Geology 12(6), 827–840.

Morrison, J., Anderson, J.L., 1998. Footwall refrigeration along a detachment fault: implications for thermal evolution of core complexes. Science 279, 63–66.

Mullis, J., 1987. Fluid inclusion studies during very low-grade metamorphism. In Low Temperature Metamorphism (ed. M. Frey). Chapman and Hall, New York, pp. 162–199.

Ohmoto, H., Rye, R.O., 1979, Isotope of sulfur and carbon, in Barnes, H. L. Ed., Geochemestry of Hydrothermal deposits, John Wiley & Sons, p. 509–567.

Parra, T., Vidal, O., Jolivet, L., 2002. Relation between deformation and retrogression in blueschist metapelites of Tinos island (Greece) evidenced by chlorite-mica local equilibria. Lithos 63, 41–66.

Passchier, C.W., Trouw, R.A.J., 2006. Microtectonics, 2nd ed. Berlin, Heidelberg, New York: Springer-Verlag. pp. 366

Pe-Piper, G., Piper, D.J.W., 2002. The igneous rocks of Greece, the anatomy of anorogen. Beiträge zur Regionalen Geologie der Erde, Gebrüder Borntraeger,Berlin–Stuttgart, Germany, pp. 573.

Petford, N., Gallagher, K., 2001. Partial melting of mafic (amphibolite) lower crust by periodic influx of basaltic magma. Earth Planetary Science Letters 193, 483–499.

Photiades, A., Carras, N., 2001. Stratigraphy and geological structure of the Lavrion area (Attica, Greece). Bulletin of the Geological Society of Greece 34, 103–109.

Ramsey, J.G., 1983. Rock ductility and its influence on the development of tectonic structures in mountain belts. In Moutain Building Processes, edited by K.J. Hsü, Academic Press, p. 111–127.

Ring, U., Layer, P.W., Reischmann, T., 2001. Miocene high-pressure metamorphism in the Cyclades and Crete, Aegean Sea, Greece: evidence for large-magnitude displacement on the Cretan detachment. Geology 29, 395–398.

Ring, U., Reischmann, T., 2002. The weak and superfast Cretan detachment, Greece: exhumation at subduction rates in extrusion wedges. Journal of the Geological Society 159, 225–228.

Ring, U., Glodny, J., Will, T., Thomson, S., 2007. An Oligocene extrusion wedge of blueschist-facies nappes on Evia, Aegean Sea, Greece: implications for the early exhumation of high-pressure rocks. Journal of the Geological Society 164, 637–652.

Ring, U., Glodny, J., Will, T. M., Thomson, S., 2011, Normal faulting on Sifnos and the South Cycladic Detachment System, Aegean Sea, Greece. Journal of the Geological Society, London 168, 751–768.

Ring, U., Glodny, J., Will, T., Thomson, S., 2010. The Hellenic subduction system: High-pressure metamorphism, exhumation, normal faulting, and large-scale extension. Annual Review of Earth and Planetary Sciences 38, 45–76.

Roedder, E., 1984. Fluid inclusions. Mineralogical Society of America. Reviews in Mineralogy 12, 644 p.

Rowe, C.D., Fagereng, A., Miller, J.A., Mapani, B., 2012. Signature of coseismic decarbonation in dolomitic fault rocks of the Naukluft Thrust, Namibia. Earth and Planetary Science Letters 333–334, 200–210.

Rye, R.O., Schuiling, R.D., Rye, D.M., Jansen, J.B.H., 1976. Carbon, hydrogen, and oxygen isotope studies of the regional metamorphic complex at Naxos, Greece. Geochimica et Cosmochimica Acta 40, 1031–1049

Scheffer, C., Vanderhaeghe, O., Lanari, P., Tarantola, A., Ponthus, L., Photiades, A., France, L., 2016. Syn- to post-orogenic exhumation of metamorphic nappes: structure and thermobarometry of the western Attic-Cycladic metamorphic complex (Lavrion, Greece). Journal of Geodynamics 96, 174–193.

Schuiling, R.D. and Kreulen, R., 1979. Are thermal domes heated by CO2-rich fluids from the mantle? Earth and Planetary Science Letters 43, 298–302.

Selverstone, J., Gutzler, D.S., 1993. Post-125 Ma carbon storage associated with continent-continent collision. Geology 21, 885–888.

Seward, D., Vanderhaeghe, O., Siebenaller, L., Thomson, S., Hibsch, C., Zinff, A., Holzner, P., Ring, U., Duchêne, S., 2009. Cenozoic tectonic evolution of Naxos Island through a multifaceted approach of fission-track analysis. Geological Society of London Special Publications 321, 179–196.

Siebenaller, L., Boiron, M.C., Vanderhaeghe, O., Hibsch, C., Jessell, M.W., Andremayer, A.S., France-Lanord, C., Photiades, A., 2013. Fluid record of rock exhumation across the brittle ductile transition during formation of a Metamorphic Core Complex (Naxos Island, Cyclades, Greece). Journal of Metamorphic Geology 31, 313–338.

Siebenaller, L., Vanderhaeghe, O., Jessell, M., Boiron, M.-C., Hibsch, C., 2016. Syntectonic fluids redistribution and circulation coupled to quartz recrystallization in the ductile crust (Naxos Island, Cyclades, Greece). Journal of Geodynamics (in press) http://dx.doi.org/10.1016/j.jog.2016.07.001.

Skarpelis, N., 2002. Geodynamics and evolution of the Miocene mineralization inthe Cycladic-Pelagonian belt, Hellenides. Bulletin of the Geological Society of Greece 34, 2191–2206.

Skarpelis, N., Luders, V., Banks, D.A., 2007. Fluid inclusions, REE and sulfur isotope geochemistry of the Lavrion carbonate hosted ore deposit, SE Attica, Greece. Geochimica et Cosmochimica Acta 71, A945–A945.

Sterner, S.M., Hall, D.L., Bodnar, R.J., 1988. Synthetic fluid inclusions. V. Solubility relations in the system NaCl-KCl-H_2O under vapor saturated conditions. Geochimica et Cosmochimica Acta 52, 989–1005.

Stöckhert, B., Brix, M.R., Kleinschrodt, R., Hurford, A.J., Wirth, R., 1999. Thermochronometry and microstructures of quartz–a comparison with experimental flow laws and predictions on the temperature of the brittle-plastic transition. Journal of Structural Geology 21, 351–369.

Stipp, M., Stünitz, H., Heilbronner, R., Schmid, S.M., 2002a. Dynamic Recrystallization of quartz: Correlation between Natural and Experimental Conditions. In: S. de Meer, M. R. Drury, J. H. P. de Bresser & G. M. Pennock: Deformation Mechanisms, Rheology and

Tectonics: Current Status and Future Perspectives. - Geological Society, London, Special Publications 200, 171-190.

Stipp, M., Stünitz, H., Heilbronner, R., Schmid, S.M., 2002b. The eastern Tonale fault zone: a “natural laboratory” for crystal plastic deformation of quartz over a temperature range from 250 - 700° C. Journal of Structural Geology 24, 1861-1884.

Tarantola, A., Mullis, J., Vennemann, T., Dubessy, J., de Capitani, C., 2007. Oxidation of methane at the CH_4/H_2O–(CO_2) transition zone in the external part of the Central Alps, Switzerland: evidences from stable isotope investigations. Chemical Geology 237, 329–357.

Tarantola, A., Mullis, J., Guillaume, D., Dubessy, J., de Capitani, C., Adbelmoula, M., 2009. Oxidation of CH4 to CO2 and H2O by chloritization of detrital biotite at 270 C in the external part of the Central Alps, Switzerland. Lithos 112, 497–510.

Tarantola, A, Diamond, L.W., Stunitz, H., 2010. Modification of fluid inclusions in quatz by deviatoric stress. I: experimentally induced changes in inclusion shape and microstructures. Contributions to mineralogy and petrology 160, 825–843.

Tarantola, A, Diamond, L.W., Stunitz, H., Thust, A., Pec, M., 2012. Modification of fluid inclusions in quartz by deviatoric stress. III: Influence of principal stresses on inclusion density and orientation. Contributions to mineralogy and petrology 164, 537–550.

Tombros, S., Seymour, K.S., Spry, P.G., Bonsall, T.A., 2010. The isotopic signature of the mineralizing fluid of the Lavrion carbonate-replacement Pb-Zn-Ag district. Bulletin of the Geological Society of Greece XLIII, 2406–2416.

Touret, J.L.R.., 1971. Le facies granulite en Norvege meridionale. II. Les inclusions fluides. Lithos 4, 423–436.

Touret, J.L.R., 2001. Fluids in metamorphic rocks. Lithos 55,1–25

Touret, J.L.R., 1992. CO_2 transfer between the upper mantle and the atmosphere: temporary storage in the lower continental crust. Terra Nova 4, 87–98.

Trotet, F., Vidal, O., Jolivet, L., 2001. Exhumation of Syros and Sifnos metamorphic rocks (Cyclades, Greece): New constraints on the P–T paths. European Journal of Mineralogy 13, 901–920.

Trull, T., Nadeau, S., Pineau, F., Polvé, M., Javoy, M., 1993. C-He systematics in hotspot xenoliths: Implications for mantle carbon contens and carbon recycling. Earth and Planetary Science Letters 118, 43–64.

Tsokas, G.N., Stampolidis, A., Angelopoulos, A.D., Kilias, S., 1998. Analysis and potential field anomalies in Lavrion mining area, Greece. Geophysics 63, 1965–1970.

Upton, P., Koons, P.O., Chamberlain, C.P., 1995. Penetration of deformation-driven meteoric water into ductile rocks: isotopic and model observations from the Southern Alps, New Zealand. New Zealand Journal of Geology and Geophysics 38, 535–543.

Urai, J.L., Means, W.D., Lister, G.S., 1986. Dynamic recrystallization of minerals. In: Hobbs, B.E., Heard H.C. (Eds.), Mineral and Rock Deformation: Laboratory Studies. Geophysical Monograph 36, 161–199.

Valley, J.W., 1986. Stable isotope geochemistry in metamorphic rocks. In stable istopes in high temperature geological processes (J.W Valley, H.P. Taylor, Jr. & J.R. O'Neil,eds.) Review in Mineralogy and Geochemistry 16, 445–490.

Vanderhaeghe, O., 2012. Thermal-mechanical evolution of orogenic belts at convergent plate boundaries: a reappraisal of the orogenic cycle, Journal of Geodynamics, 56-57, pp. 124-145

Vanderhaeghe, O., Hibsch, C., Siebenaller, L., Martin, L., Duchêne, S., de St Blanquat, M., Kruckenberg, S., Fotiadis, A., 2007. Penrose Conference – Extending a continent – Naxos Field guide. In (eds) Lister G., Forster M., and Ring U., Inside the Aegean Metamorphic Core Complexes, Journal of the Virtual Explorer, Electronic Edition, ISSN 1441-8142, Volume 27, Paper 4.

Vanderhaeghe, O., 2004. Structural development of the Naxos migmatite dome. Geological Society of America: Special Paper 380, 211–227.

Vanderhaeghe, O., Teyssier, C., 2001. Partial melting and the flow of orogens. Tectonophysics 342, 451–472.

Vanderhaeghe, O., Duchêne, S., 2010. Crustal-scale mass transfer, geotherm and topography at convergent plate boundaries. Terra Nova 22, 315–323.

Vanderhaeghe, O., Medvedev, S., Fullsack, P., Beaumont, C., Jamieson, R.A., 2003. Evolution of orogenic wedges and continental plateaux: insights from crustal thermal–mechanical models overlying subducting mantle lithosphere. Geophysical Journal International 153 (1), 27–51.

Vapnik, Y., Avigad, D., 2004. P-T conditions of quartz-calcite boudins and vein formation within a low-angle detachment fault in Tinos Island (Aegean Sea): a fluid inclusion study. International Journal of Earth Sciences 93, 487–499.

Vernooij, M.G.C., Langenhorst, F., 2005. Experimental reproduction of tectonic deformation lamellae in quartz and comparison to shock-induced planar deformation features. Meteoritics & Planetary Science 40 (9/10), 1353–361.

Voudouris, P., Melfos, V., Spry, P.G., Bonsall, T., Tarkian, M., Economou-Eliopoulos, M., 2008a. Mineralogical and fluid inclusion constraints on the evolution of the Plaka intrusion-related ore system, Lavrion, Greece. Mineralogy and Petrology 93, 79–110.

Voudouris, P., Melfos, V., Spry, P.G., Bonsall, T.A., Tarkian, M., Solomos, C., 2008b. Carbonate replacement Pb–Zn–Ag ± Au mineralization in the Kamariza area, Lavrion, Greece: Mineralogy and thermochemical conditions of formation. Mineralogy and Petrology 94, 85–106.

Wickham, S.M., Peters, M.T., Fricke, H.C., O'Neil, J.R., 1993. Identification of magmatic and meteoric fluid sources and upward- and downward-moving infiltration fronts in a metamorphic core complex. Geology 21, 81–84.

Wilkins, R.W.T., Barkas, J.P., 1978. Fluid inclusions, deformation and recrystallization in granite tectonites. Contributions to Mineralogy and Petrology 65, 293–299.

Yardley, B.W.D., Bodnar, R.J., 2014. Fluids in the continental crust. Geochemical Perspectives 3 (1), 123 p.

Zhang, Y.G., Frantz, J.D., 1987. Determination of the homogenization temperatures and densities of supercritical fluids in the system NaCI-KCI-CaCI$_2$-H$_2$O using synthetic fluid inclusions. Chemical Geology 64, 335–350.

Zheng, Y.F., 1999. Oxygen isotope fractionation in carbonate and sulfate minerals. Geochemical Journal 33, 109–126.

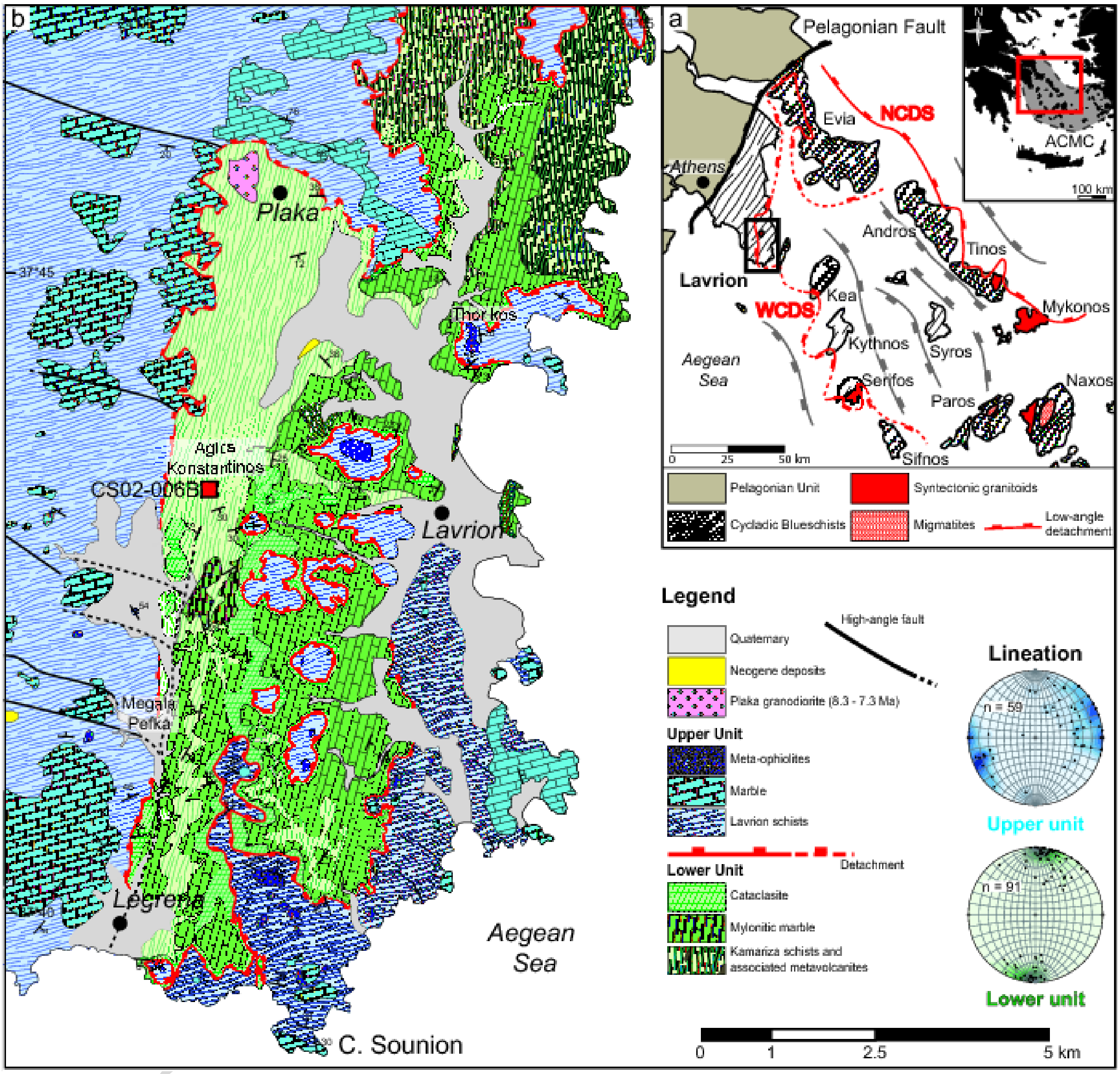
b
Plaka
37°45
Thorikos
Agios Konstantinos
CS02-006B
Lavrion
Megala Pefka
Legrena
Aegean Sea
C. Sounion
a
Pelagonian Fault
Evia
NCDS
Athens
Andros
Tinos
Lavrion
WCDS
Kea
Mykonos
Kythnos
Syros
Aegean Sea
Serifos
Paros
Naxos
Sifnos
0 25 50 km
N
ACMC
100 km
Pelagonian Unit
Syntectonic granitoids
Cycladic Blueschists
Migmatites
Low-angle detachment
Legend
High-angle fault
Quaternary
Neogene deposits
Plaka granodiorite (8.3 - 7.3 Ma)
Upper Unit
Meta-ophiolites
Marble
Lavrion schists
Detachment
Lower Unit
Cataclasite
Mylonitic marble
Kamariza schists and associated metavolcanites
Lineation
n = 59
Upper unit
n = 91
Lower unit
0 1 2.5 5 km

Figure 1

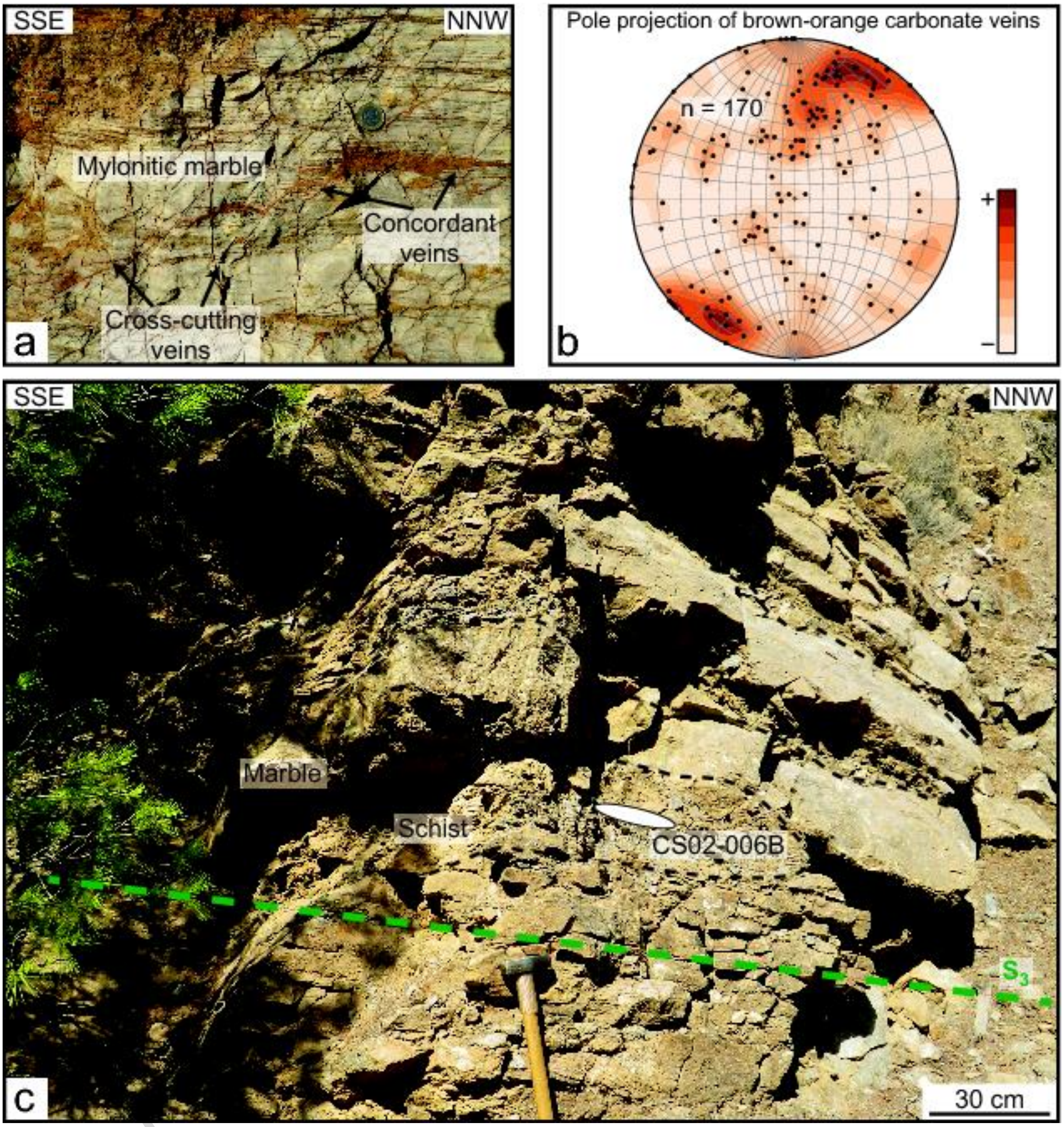
SSE
NNW
Mylonitic marble
Concordant veins
Cross-cutting veins
a
Pole projection of brown-orange carbonate veins
n = 170
+
–
b
SSE
NNW
Marble
Schist
CS02-006B
S3
c
30 cm

Figure 2

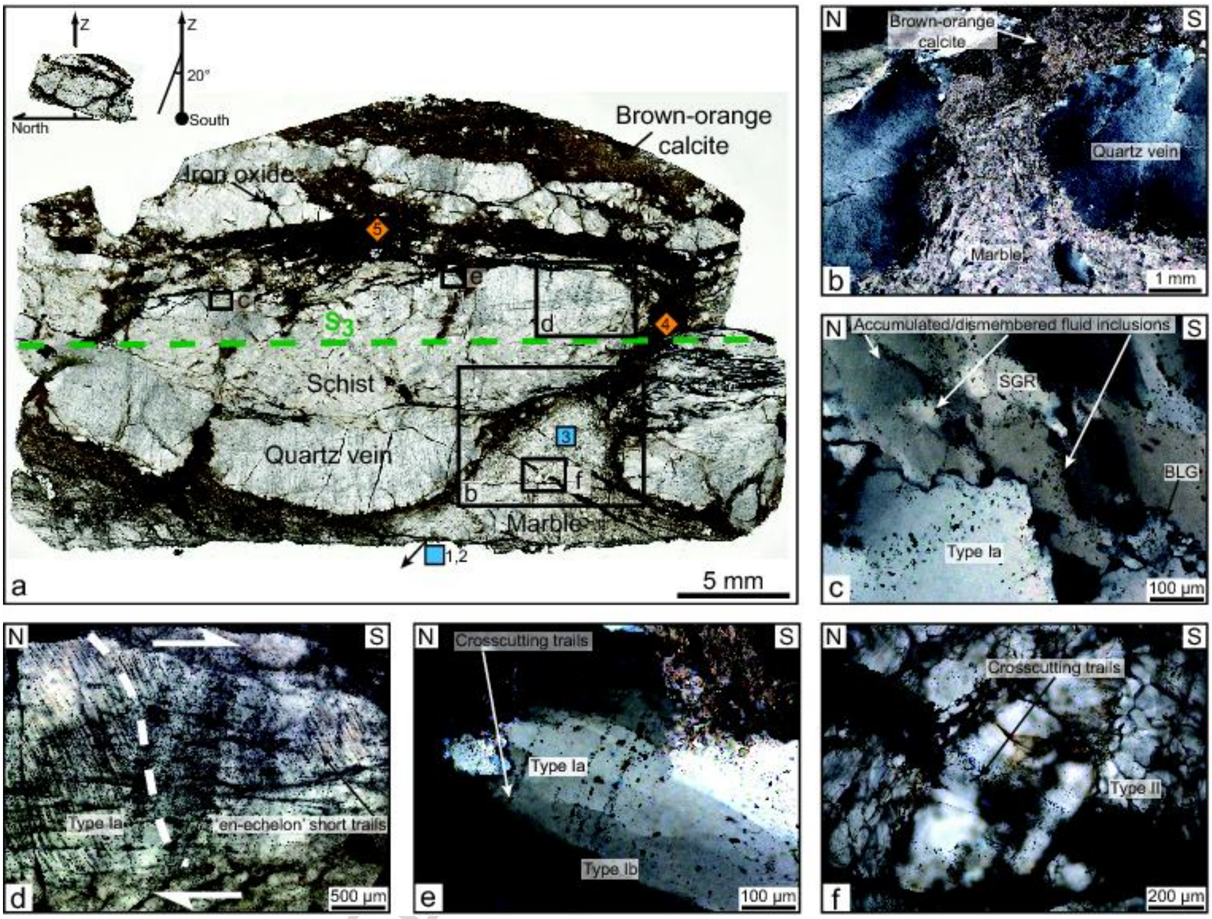
z
North
z
20°
South
Brown-orange calcite
Iron oxide
5
e
c
d
4
S3
Schist
Quartz vein
3
b
f
Marble
1,2
a
5 mm
N
S
Brown-orange calcite
Quartz vein
Marble
b
1 mm
N
Accumulated/dismembered fluid inclusions
S
SGR
BLG
Type Ia
c
100 μm
N
S
Type Ia
'en-echelon' short trails
d
500 μm
N
Crosscutting trails
S
Type Ia
Type Ib
e
100 μm
N
S
Crosscutting trails
Type II
f
200 μm

Figure 3

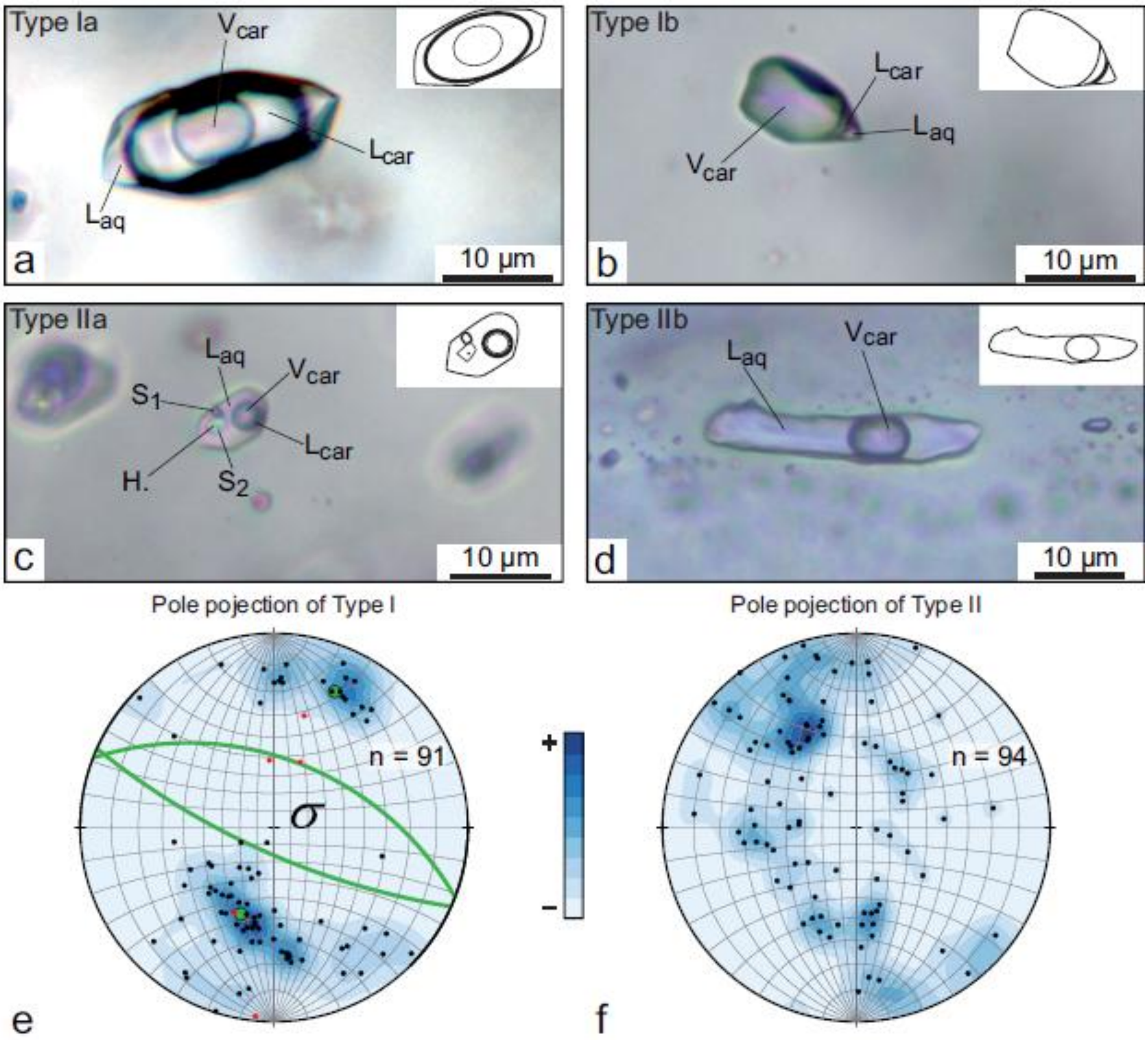
Type Ia
V_{car}
L_{car}
L_{aq}
a
10 µm
Type Ib
L_{car}
L_{aq}
V_{car}
b
10 µm
Type IIa
L_{aq}
V_{car}
S_1
L_{car}
H.
S_2
c
10 µm
Type IIb
L_{aq}
V_{car}
d
10 µm
Pole pojection of Type I
n = 91
σ
+
–
Pole pojection of Type II
n = 94
e
f

Figure 4

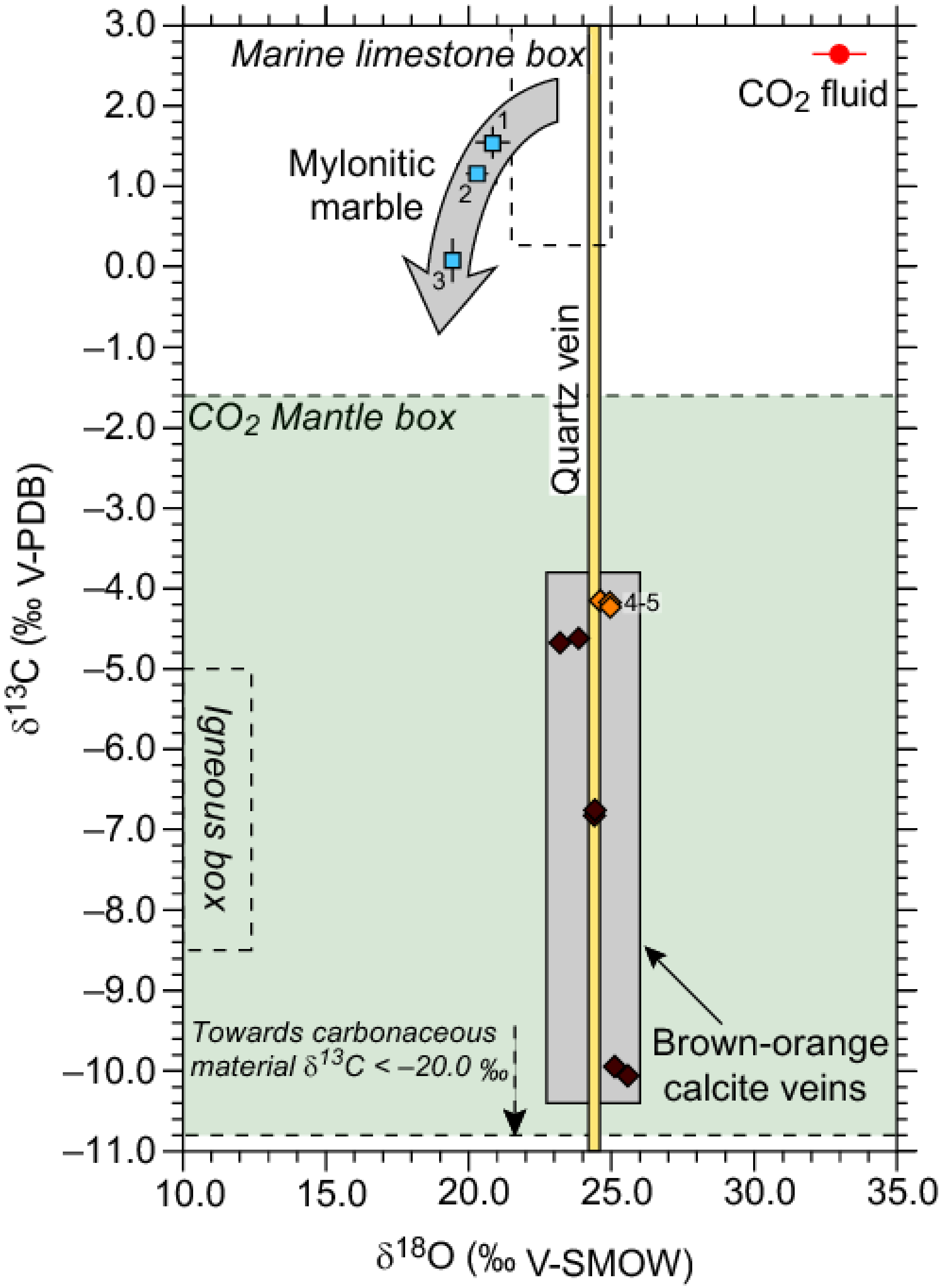
Marine limestone box
CO2 fluid
Mylonitic marble
1
2
3
Quartz vein
CO2 Mantle box
4-5
Igneous box
Towards carbonaceous material δ13C < –20.0 ‰
Brown-orange calcite veins
δ13C (‰ V-PDB)
δ18O (‰ V-SMOW)
3.0
2.0
1.0
0.0
–1.0
–2.0
–3.0
–4.0
–5.0
–6.0
–7.0
–8.0
–9.0
–10.0
–11.0
10.0
15.0
20.0
25.0
30.0
35.0

Figure 5

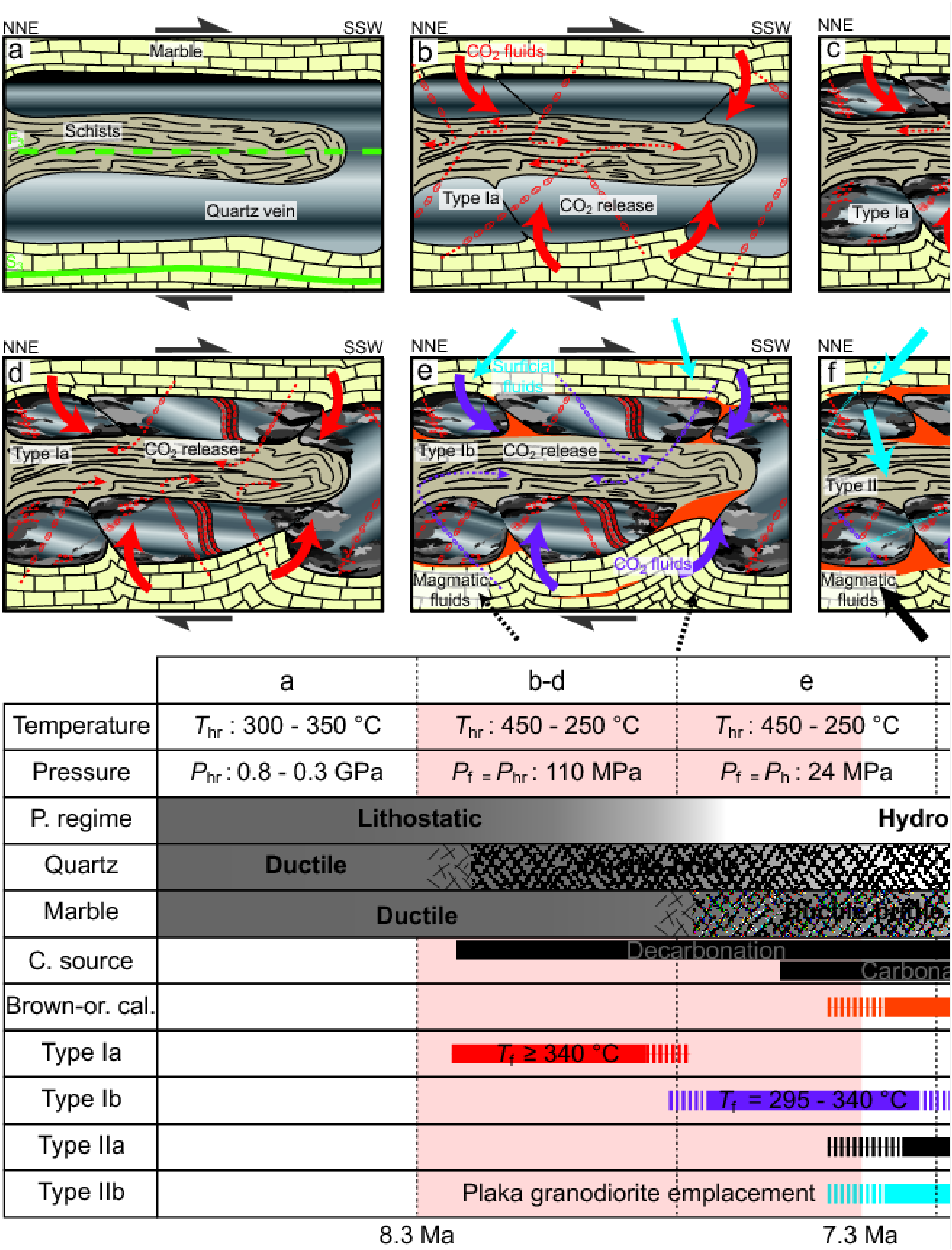

	a	b-d	e
Temperature	T_{hr} : 300 - 350 °C	T_{hr} : 450 - 250 °C	T_{hr} : 450 - 250 °C
Pressure	P_{hr} : 0.8 - 0.3 GPa	$P_f = P_{hr}$: 110 MPa	$P_f = P_h$: 24 MPa
P. regime	Lithostatic		Hydro
Quartz	Ductile	Ductile-brittle	
Marble	Ductile		Ductile-brittle
C. source		Decarbonation	Carbona
Brown-or. cal.			
Type Ia		$T_f \geq 340$ °C	
Type Ib			T_f = 295 - 340 °C
Type IIa			
Type IIb		Plaka granodiorite emplacement	

8.3 Ma

7.3 Ma

Figure 6

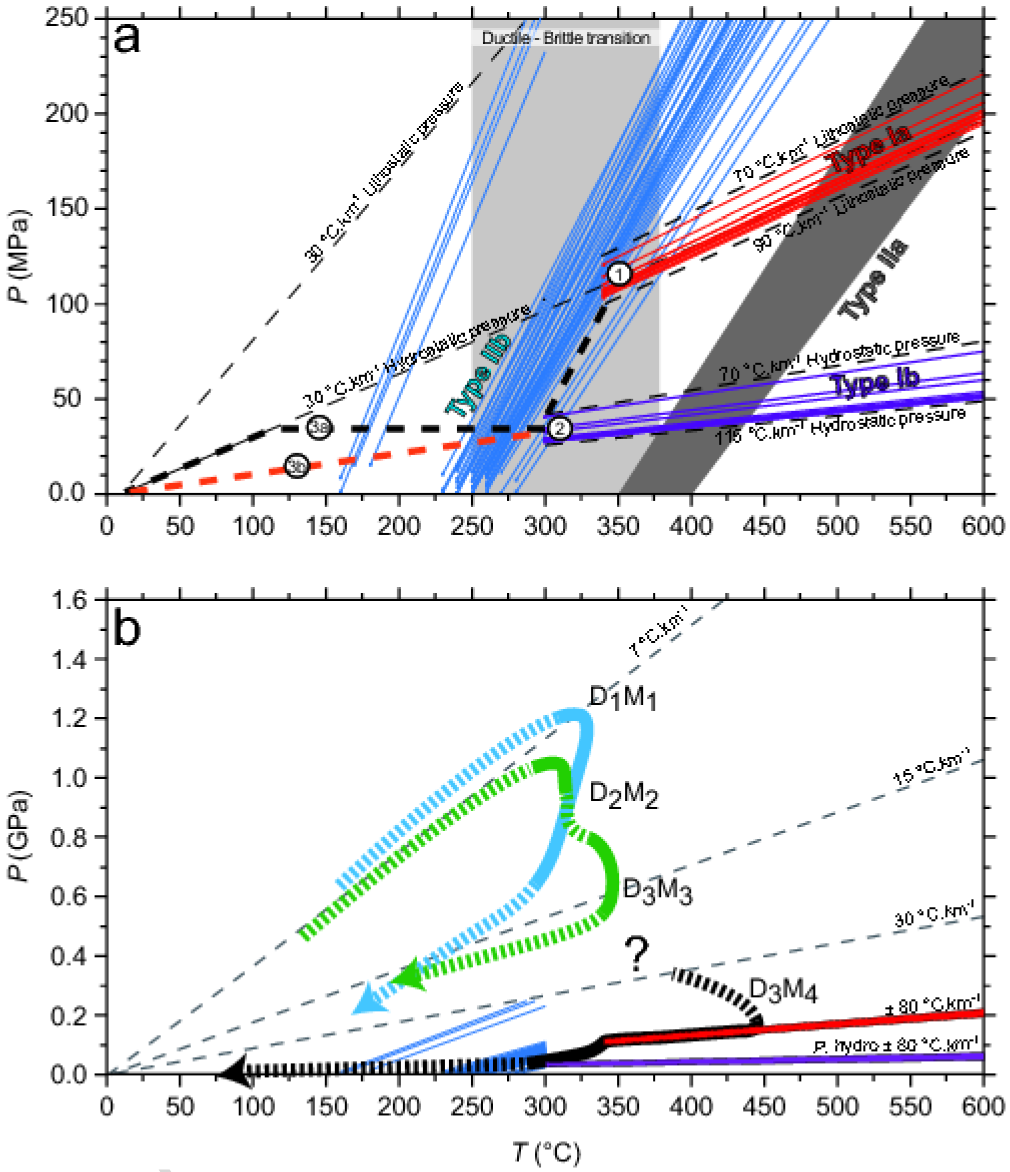
a
Ductile - Brittle transition
30 °C.km-1 Lithostatic pressure
70 °C.km-1 Lithostatic pressure
90 °C.km-1 Lithostatic pressure
30 °C.km-1 Hydrostatic pressure
70 °C.km-1 Hydrostatic pressure
115 °C.km-1 Hydrostatic pressure
Type Ia
Type Ib
Type IIa
Type IIb
1
2
3a
3b
P (MPa)
250
200
150
100
50
0.0
b
7 °C.km-1
15 °C.km-1
30 °C.km-1
± 80 °C.km-1
P. hydro ± 80 °C.km-1
D1M1
D2M2
D3M3
D3M4
?
P (GPa)
1.6
1.4
1.2
1.0
0.8
0.6
0.4
0.2
0.0
0
50
100
150
200
250
300
350
400
450
500
550
600
T (°C)

Figure 7

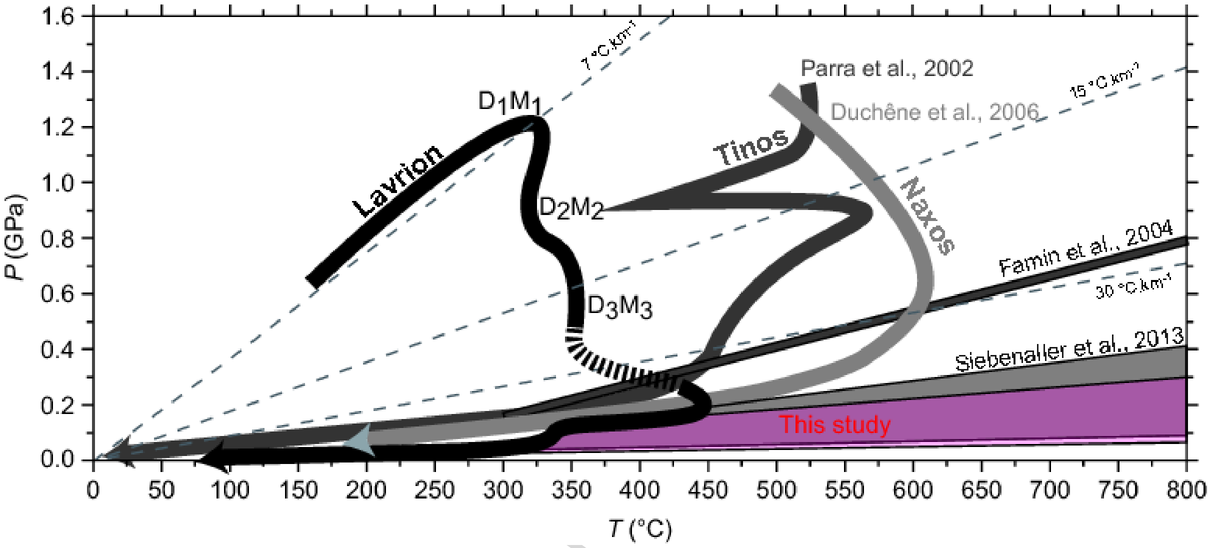
1.6
1.4
1.2
1.0
0.8
0.6
0.4
0.2
0.0
P (GPa)
0
50
100
150
200
250
300
350
400
450
500
550
600
650
700
750
800
T (°C)
7 °C.km-1
15 °C.km-1
30 °C.km-1
Parra et al., 2002
Duchêne et al., 2006
D1M1
D2M2
D3M3
Lavrion
Tinos
Naxos
Famin et al., 2004
Siebenaller et al., 2013
This study

Figure 8

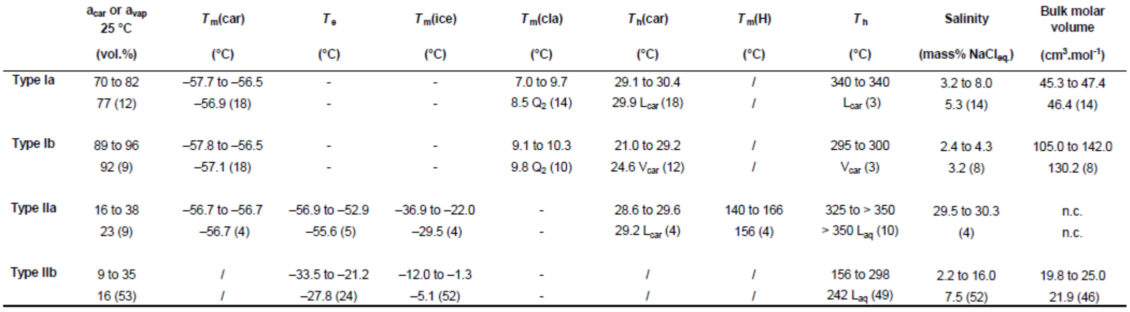

	a_{car} or a_{vap} 25 °C (vol.%)	T_m(car) (°C)	T_e (°C)	T_m(ice) (°C)	T_m(cla) (°C)	T_h(car) (°C)	T_m(H) (°C)	T_h (°C)	Salinity (mass% $NaCl_{eq.}$)	Bulk molar volume ($cm^3.mol^{-1}$)
Type Ia	70 to 82	–57.7 to –56.5	-	-	7.0 to 9.7	29.1 to 30.4	/	340 to 340	3.2 to 8.0	45.3 to 47.4
	77 (12)	–56.9 (18)	-	-	8.5 Q_2 (14)	29.9 L_{car} (18)	/	L_{car} (3)	5.3 (14)	46.4 (14)
Type Ib	89 to 96	–57.8 to –56.5	-	-	9.1 to 10.3	21.0 to 29.2	/	295 to 300	2.4 to 4.3	105.0 to 142.0
	92 (9)	–57.1 (18)	-	-	9.8 Q_2 (10)	24.6 V_{car} (12)	/	V_{car} (3)	3.2 (8)	130.2 (8)
Type IIa	16 to 38	–56.7 to –56.7	–56.9 to –52.9	–36.9 to –22.0	-	28.6 to 29.6	140 to 166	325 to > 350	29.5 to 30.3	n.c.
	23 (9)	–56.7 (4)	–55.6 (5)	–29.5 (4)	-	29.2 L_{car} (4)	156 (4)	> 350 L_{aq} (10)	(4)	n.c.
Type IIb	9 to 35	/	–33.5 to –21.2	–12.0 to –1.3	-	/	/	156 to 298	2.2 to 16.0	19.8 to 25.0
	16 (53)	/	–27.8 (24)	–5.1 (52)	-	/	/	242 L_{aq} (49)	7.5 (52)	21.9 (46)

Table 1

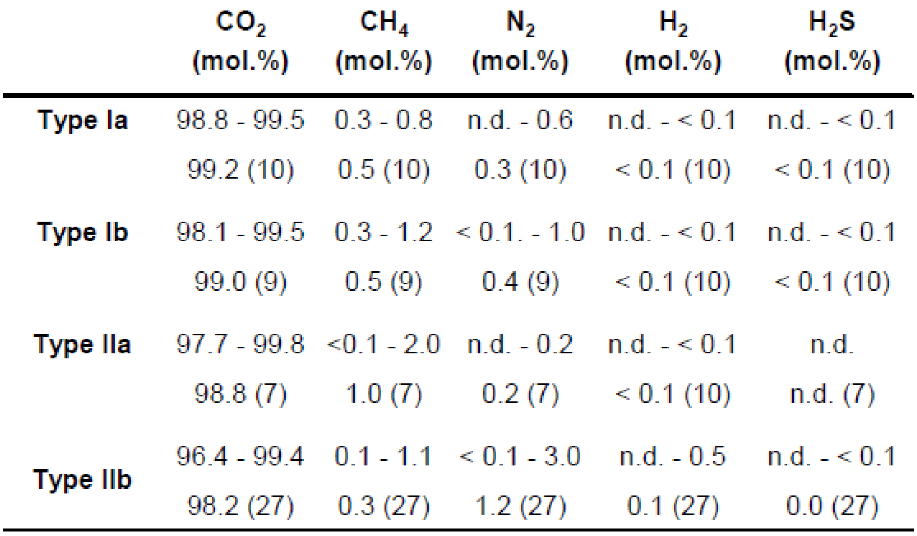

	CO_2 (mol.%)	CH_4 (mol.%)	N_2 (mol.%)	H_2 (mol.%)	H_2S (mol.%)
Type Ia	98.8 - 99.5	0.3 - 0.8	n.d. - 0.6	n.d. - < 0.1	n.d. - < 0.1
	99.2 (10)	0.5 (10)	0.3 (10)	< 0.1 (10)	< 0.1 (10)
Type Ib	98.1 - 99.5	0.3 - 1.2	< 0.1. - 1.0	n.d. - < 0.1	n.d. - < 0.1
	99.0 (9)	0.5 (9)	0.4 (9)	< 0.1 (10)	< 0.1 (10)
Type IIa	97.7 - 99.8	<0.1 - 2.0	n.d. - 0.2	n.d. - < 0.1	n.d.
	98.8 (7)	1.0 (7)	0.2 (7)	< 0.1 (10)	n.d. (7)
Type IIb	96.4 - 99.4	0.1 - 1.1	< 0.1 - 3.0	n.d. - 0.5	n.d. - < 0.1
	98.2 (27)	0.3 (27)	1.2 (27)	0.1 (27)	0.0 (27)

Table 2

Sample	$\delta^{13}C$ (‰ V-PDB)	$\delta^{18}O$ (‰ V-SMOW)
Thin section scale		
Marble_1	1.2	19.9
	1.1	20.7
Marble_2	1.7	21.4
	1.3	20.3
Marble_3	0.4	19.2
	–0.2	19.7
B.Orange calcite_4	–4.2	24.6
	–4.2	25.0
B.Orange calcite_5	–4.2	25.0
Quartz vein	-	24.2
	-	24.5
CO_2	2.6	33.8
	2.7	31.9
Outcrop scale		
B.Orange calcite	–9.9	25.1
	–10.0	25.5
B.Orange calcite	–4.7	23.2
	–4.6	23.8
B.Orange calcite	–6.8	24.3
	–6.7	24.4

Table 3